Spatial and frequency identification of the dynamic properties of thin plates with the Frequency-Adapted Virtual Fields Method

Nicolas Madinier, Quentin Leclère, Kerem Ege, Alain Berry

Spatial and frequency identification of the dynamic properties of thin plates with the Frequency-Adapted Virtual Fields Method

Nicolas Madinier[a,b,*], Quentin Leclère[a], Kerem Ege[a] and Alain Berry[b]

[a]Laboratoire Vibrations Acoustique, INSA Lyon, 25 bis avenue Jean Capelle F-69621 Villeurbanne Cedex, FRANCE
[b]Centre de Recherche Acoustique - Signal - Humain, Université de Sherbrooke, 2500 Boulevard de l'Université, Sherbrooke (QC), CANADA

ABSTRACT

Vibroacoustic inverse methods use the measured response of a vibrating structure to identify a structural parameter or a dynamic load. Two inverse methods are considered, the Force Analysis Technique (FAT) and the Virtual Fields Method (VFM). The Corrected Force Analysis Technique (CFAT) is a variant of FAT that corrects its singularity. This correction allows the method to be applied in the high-frequency domain, when the number of measurement points per flexural wavelength becomes small. In this study, the proposed novelty is the development of a Frequency-Adapted VFM (FA VFM) to the case of a Love-Kirchhoff plate. Thanks to this method, the VFM can now be applied to identify the equivalent bending stiffness and structural damping of a thin plate when the number of measurement points per wavelength is small. The method has previously been developed for an Euler-Bernoulli beam. An experimental identification of the complex bending stiffness of an locally damped aluminium plate using Laser Doppler Velocimetry (LDV) data and the developed method is performed. The experimental study shows for the first time that the FA VFM can be used to map the equivalent bending stiffness and structural damping as a function of position on a plate and identify these parameters as a function of frequency over a large frequency band. The results of the Frequency-Adapted VFM are compared with those of CFAT and the classical VFM approach. FA VFM results are more accurate than those of classical VFM and similar to those of CFAT.

1. Introduction

The development of new materials that offer good mechanical strength for minimum weight, such as composite or multi-layer panels, is now a major challenge in certain industrial sectors. These new developments lead to the need for bending stiffness and loss factor identification in order to solve direct vibro-acoustic problems or complete numerical models that will resolve the direct problem [1]. In vibroacoustics, the mechanical characterisation of materials can be carried out in different ways. A first approach is to use modal analysis to determine bending stiffness and damping at low frequencies. The Estimation of Signal Parameters via Rotational Invariance Techniques (ESPRIT) method decomposes the response of the structure into a sum of complex exponentials plus Gaussian noise to perform a modal analysis at higher frequencies. The method can be used as long as the modal overlap remains below 70% [2]. However, modal analysis only allows characterisation at the structure's natural frequencies and to do this, the structure must first be modelled [3]. Inverse vibratory methods can then be used to characterize the structure over a wider frequency band. These methods analyse the vibratory response of the structure to identify the complex bending stiffness. A number of inverse methods can be used depending on the frequency range under consideration. Methods such as High-Resolution Wave-vector Analysis (HRWA) [4] which has been used to identify the local bending stiffness of a complex structure or the Algebraic Wavenumber Identification (AWI) [5] are designed to extract the wavenumbers of the structure. Some of these methods are global, such as Inhomogeneous Wave Correlation (IWC), which considers that the response of the structure can be described using a plane wave. The complex bending stiffness is determined by fitting this model to the actual response of the structure [6, 7]. The model used in the IWC is too imprecise close to the sources. It is made more complex using Hankel functions [8, 7]. It should be noted that inverse methods can also be used to characterize other structures. For example, in [9, 10], the parameters of the constitutive equation of inhomogeneous viscoelastic material are identified and mapped.

*Corresponding author at: Centre de Recherche Acoustique - Signal - Humain, Université de Sherbrooke, 2500 Boulevard de l'Université, Sherbrooke (QC), Canada.
nicolas.madinier@usherbrooke.ca (N. Madinier)
ORCID(s): 0009-0007-9180-7369 (N. Madinier)

Nomenclature

A_i and B_i	Polynomial function of τ used in the expression of $\tilde{p}^{\mathrm{VFM}}(x_i, y_i)$
$\mathbf{B}$ and $\mathbf{N}$	Column vectors used in the least squares calculation
D	Complex Bending stiffness
$(D/(\rho h))^{\mathrm{FAT}}_{(x_i,y_i)}$, $(D/(\rho h))^{\mathrm{CFAT}}_{(x_i,y_i)}$, $(D/(\rho h))^{\mathrm{VFM}}_{(x_i,y_i)}$	Complex Bending stiffness identified with FAT, CFAT and the VFM at point (x_i, y_i)
E	Young Modulus
E^{FAT}, E^{CFAT} and E^{VFM}	Response of FAT, CFAT and the VFM in the wavenumber domain
h	Thickness of the plate
H_1 and H_2	Hermite16 interpolation functions
H	Response of the low-pass wavenumber filter
$k_{\mathrm{f}} = 2\pi/\lambda_{\mathrm{f}} = \sqrt[4]{(\rho h \omega^2)/D}$	Flexural wavenumber of the plate
k_c	Cut-off wavenumber of the low-pass wavenumber filter
K_x^P and K_y^P	Polynomial interpolation of the curvatures
$n = 2\pi/(k_{\mathrm{f}}\Delta)$	Number of measurement points per wavelength
$p(x, y, t) = \tilde{p}(x, y)e^{\mathrm{j}\omega t}$	Harmonic transverse loading in N/m^2
$\tilde{p}^{\mathrm{FAT}}(x_i, y_i)$, $\tilde{p}^{\mathrm{CFAT}}(x_i, y_i)$ and $\tilde{p}^{\mathrm{VFM}}(x_i, y_i)$	Load estimated by FAT, CFAT and the VFM at point (x_i, y_i)
$\hat{p}(k_x, k_y)$, $\hat{p}^{\mathrm{FAT}}(k_x, k_y)$ and $\hat{p}^{\mathrm{VFM}}(k_x, k_y)$	Fourier transform of $\tilde{p}(x, y)$, $\tilde{p}^{\mathrm{FAT}}(x, y)$ and $\tilde{p}^{\mathrm{VFM}}(x, y)$
$\mathbf{P}$	Matrix used to calculate $W^P(\xi, \psi)$
$p^{(i)}_{l,o}$	Elements of $\mathbf{P}$
S_v	Virtual Window
$\tilde{w}(x, y)$	Out of the plane displacement of the plate
$\tilde{w}_{o,l}$	Displacement measured at the point $\tilde{w}(x_i + o\Delta, y_i + l\Delta)$.
$\hat{w}(k_x, k_y)$	Fourier transform of $\tilde{w}(x, y)$
$w^v(x, y)$	Virtual displacement
$W^P(\xi, \psi)$	Polynomial interpolation of the displacement
$\gamma^{00}_{(x_i,y_i)}$, $\gamma^{10}_{(x_i,y_i)}$, $\gamma^{20}_{(x_i,y_i)}$, $\gamma^{11}_{(x_i,y_i)}$ and $\gamma^{22}_{(x_i,y_i)}$	Linear combinations of the 25 measured displacement values of the subset used in the polynomial interpolation
$\delta^{4x}_{\Delta}(x_i, y_i)$, $\delta^{4y}_{\Delta}(x_i, y_i)$, $\delta^{2x2y}_{\Delta}(x_i, y_i)$	Estimation of the fourth-order spatial derivatives of $\tilde{w}(x)$ by the finite differences scheme
Δ	Distance between two measurement points
η	Loss factor
$\tilde{\kappa}_x(x, y)$ and $\tilde{\kappa}_y(x, y)$	Bending curvatures of the plate
$\kappa^v_x(x, y)$ and $\kappa^v_y(x, y)$	Virtual curvatures
μ^4 and ν^4	Corrective factors of CFAT
μ	Mass per unit of area
ν	Poisson's ratio
$\boldsymbol{\psi}$	Matrix used to calculate $W^P(\xi, \psi)$
ρ	Density
τ	Half length of the edge of the virtual window
τ^i_{FA}	Frequency-Adapted value of the half length of the virtual window calculated when the angular direction i on the circle $\sqrt{k_x^2 + k_y^2} = k_{\mathrm{f}}$ is chosen to eliminate the singularity
ξ and ψ	Local coordinate system on the virtual window
$\boldsymbol{\xi}$ and $\boldsymbol{\psi}$	Matrices used to calculate $W^P(\xi, \psi)$
ω	Angular frequency

Most of these methods can be used to characterise the structure locally if the analysis is carried out on a small part of the vibration field. Some inverse methods, such as the Force Analysis Technique (FAT) or the Virtual Fields Method (VFM), use a local approach. These two methods will be investigated in this study.

The Force Analysis Technique was first developed to identify dynamic forces using the local equation of motion. The method uses a finite difference scheme to estimate the fourth-order spatial derivatives of the displacement field in the local equation of motion. The method has been applied to beams [11] and plates [12]. FAT has been extended to identify the bending stiffness and loss factor of an isotropic plate [1] and of an orthotropic plate [13]. In [14], the method is also applied to identify the bending stiffness and shear moduli of a sandwich beam. One of the strengths of the method is its local approach. However, estimating the spatial derivatives of the displacement amplifies the measurement noise. In addition, the error in the method due to the estimation of the derivatives with the finite difference scheme becomes significant when the number of measurement points becomes too small. To solve the first problem, windowing and filtering operations are commonly used to help regularize the problem. The Corrected Force Analysis Technique (CFAT) is a variant of FAT that corrects the bias of the finite difference pattern that appears at high frequencies. Like FAT, CFAT was first developed to identify dynamic forces [15] but it has also been extended to identify the bending stiffness of an isotropic plate [16]. More recently, the method has been extended to more complex panels to identify dynamic forces [17] and bending stiffness [3, 18].

The VFM has been developed for the static or dynamic characterization of materials using full-field measurements. The VFM is based on the Principle of Virtual Work (PVW) and consists of choosing a test function called virtual field to solve the PVW. The VFM has been used to identify the complex bending stiffness of an isotropic structure [19, 20], of an orthotropic structure [21, 22] and of anistropic structures [23, 24]. The method has been applied to identify a complex stiffness distribution [25] or damages into composite plate [26]. The choice of the virtual fields is a key point in the method since this choice can affect the accuracy of the results. In [27], virtual fields defined as optimized were developed. These virtual fields are used to minimise the effect of measurement noise in the problem. These optimized virtual fields have been widely used. For example, in [28] to identify the structural parameters of a vibrating plate or in [29] to estimate the parameters of viscoelastic materials. In [30] the parameters of a plastic model are identified using an extension of these optimized virtual fields. It is important to note, however, that these optimised virtual fields are dependent on the vibratory response of the structure. This is a drawback of this method. The VFM can be applied using piecewise virtual fields that are defined only over a small area called a virtual window. The PVW is then solved locally. This approach has been used mainly to identify dynamic loads in the frequency domain [31, 32] and in the time domain [33, 34]. However, it has not yet been applied to identify the complex bending stiffness of a plate over a wide frequency band. The use of the virtual window adds a local aspect to the method and will be used below. It should be highlighted that this local aspect is one of the main advantages of the method. This allows the method to be implemented without any a priori knowledge of the boundary conditions of the plate. In [35], a VFM frequency adaptation process for the identification of dynamic forces and bending stiffness for an Euler-Bernoulli beam has been proposed. The Frequency-Adapted Virtual Fields Method (FA VFM) enables the VFM to be applied in the high-frequency domain. The frequency adaptation process consists in finding a Frequency-Adapted value for the integration interval in the PVW.

In this paper, the proposed novelty is an extension to the 2D case of the FA VFM for identifying the equivalent bending stiffness and loss factor of a bending plate and the inclusion of experimental validations. Thanks to this extension, the characterisation of a Love-Kirchhoff plate using the VFM is possible over a large frequency range. The FA VFM process uses polynomial interpolation of the displacement field to find at each frequency a size for the virtual window which will enable the method to be applied at higher frequencies. The second section introduces FAT and the CFAT and the third one, the VFM. In the fourth section the frequency adaptation process is detailed. The fifth section presents a numerical study aimed at identifying the complex bending stiffness of a homogeneous, isotropic, highly damped and infinite Love-Kirchhoff plate with the FA VFM. Finally, in the sixth section the FA VFM is tested on experimental data presented in [16]. The plate considered in this study is locally damped using a square of foam glued to the panel. Consequently, the sixth section will demonstrate in particular the ability of FA VFM to identify spatial variations in bending stiffness and damping.

2. Force Analysis Technique and Corrected Force Analysis Technique

2.1. Force Analysis Technique

A Love-Kirchhoff plate of thickness h, density ρ, Young modulus E, Poisson's ratio ν and bending stiffness $D = Eh^3/(12(1-\nu^2))$ is subjected to a harmonic load $p(x,y,t) = \tilde{p}(x,y)e^{j\omega t}$ where ω is the angular frequency, x and y designate cartesian coordinates on the plate surface and $j = \sqrt{-1}$. Note that structural damping is modelled using a complex bending stiffness. The local equation of motion is given by [15],

$$\tilde{p}(x,y) = -\rho h\omega^2 \tilde{w}(x,y) + D\left(\frac{\partial^4 \tilde{w}(x,y)}{\partial x^4} + 2\frac{\partial^4 \tilde{w}(x,y)}{\partial x^2 \partial y^2} + \frac{\partial^4 \tilde{w}(x,y)}{\partial y^4}\right), \tag{1}$$

where $w(x,y,t) = \tilde{w}(x,y)e^{j\omega t}$ denotes the out of plane displacement of the plate. In order to identify the applied force $\tilde{p}$, the Force Analysis Technique (FAT) estimates the fourth-order spatial derivatives of $\tilde{w}(x,y)$ at the point (x_i, y_i) using a finite differences scheme based on the measured displacement [16]. This approximation is obtained using the Taylor theorem [36],

$$\begin{cases} \left.\dfrac{\partial^4 \tilde{w}}{\partial x^4}\right)_{(x_i,y_i)} \simeq \delta_\Delta^{4x}(x_i,y_i) = \dfrac{\tilde{w}_{-2,0} - 4\tilde{w}_{-1,0} + 6\tilde{w}_{0,0} - 4\tilde{w}_{1,0} + \tilde{w}_{2,0}}{\Delta^4}, \\ \left.\dfrac{\partial^4 \tilde{w}}{\partial y^4}\right)_{(x_i,y_i)} \simeq \delta_\Delta^{4y}(x_i,y_i) = \dfrac{\tilde{w}_{0,-2} - 4\tilde{w}_{0,-1} + 6\tilde{w}_{0,0} - 4\tilde{w}_{0,1} + \tilde{w}_{0,2}}{\Delta^4}, \\ \left.\dfrac{\partial^4 \tilde{w}}{\partial x^2 \partial y^2}\right)_{(x_i,y_i)} \simeq \delta_\Delta^{2x2y}(x_i,y_i) = \dfrac{1}{\Delta^4}(\tilde{w}_{-1,-1} - 2\tilde{w}_{-1,0} + \tilde{w}_{-1,1} - 2\tilde{w}_{0,-1} + 4\tilde{w}_{0,0} - 2\tilde{w}_{0,1} + \tilde{w}_{1,-1} - 2\tilde{w}_{1,0} + \tilde{w}_{1,1}). \end{cases} \tag{2}$$

where Δ is the distance between two measurement points in both directions and $\tilde{w}_{o,l} = \tilde{w}(x_i + o\Delta, y_i + l\Delta)$. The pressure at point (x_i, y_i) estimated by FAT is,

$$\tilde{p}^{\mathrm{FAT}}(x_i,y_i) = -\rho h\omega^2 \tilde{w}_(x_i,y_i) + D\left(\delta_\Delta^{4x}(x_i,y_i) + 2\delta_\Delta^{2x2y}(x_i,y_i) + \delta_\Delta^{4y}(x_i,y_i)\right), \tag{3}$$

Applying the finite difference scheme amplifies the measurement noise present at high wavenumbers. A low-pass wavenumber filter is therefore generally applied to the measured displacement. To avoid the Gibbs phenomenon, filtered fields are windowed beforehand [1]. Another problem with FAT is that the application of the finite difference scheme introduces a bias error which strongly deteriorates the results when the number of measurement points per wavelength $n = 2\pi/(k_f\Delta)$ becomes too small. Here $k_f = \sqrt[4]{\rho h\omega^2/D}$ is the flexural wavenumber of the plate. The Corrected Force Analysis Technique (CFAT) is a variant of FAT that corrects this bias error.

2.2. Corrected Force Analysis Technique

The Fourier transform of eq. (1) is [16],

$$\hat{p}(k_x,k_y) = \hat{w}(k_x,k_y)(D(k_x^2+k_y^2)^2 - \rho h\omega^2), \tag{4}$$

and that of eq. (3) is [16],

$$\hat{p}^{\mathrm{FAT}}(k_x,k_y) = \hat{w}(k_x,k_y)\left(\frac{D}{\Delta^4}(4(1-\cos(k_x\Delta))^2 + 4(1-\cos(k_y\Delta))^2 + 8(1-\cos(k_x\Delta))(1-\cos(k_y\Delta)) - \rho h\omega^2\right), \tag{5}$$

where $\hat{p}(k_x,k_y)$ and $\hat{w}(k_x,k_y)$ are the Fourier transforms of $\tilde{p}$ and $\tilde{w}$ respectively. The response of FAT in the wavenumber domain is given by,

$$E^{\mathrm{FAT}} = \frac{\hat{p}^{\mathrm{FAT}}}{\hat{p}} = \frac{\dfrac{4(1-\cos(k_x\Delta))^2 + 4(1-\cos(k_y\Delta))^2 + 8(1-\cos(k_x\Delta))(1-\cos(k_y\Delta))}{\Delta^4} - k_f^4}{(k_x^2+k_y^2)^2 - k_f^4}. \tag{6}$$

The response shows a singularity on the circle of equation $\sqrt{k_x^2 + k_y^2} = k_\mathrm{f}$. The Corrected Force Analysis Technique (CFAT) introduces two multiplying factors μ^4 and ν^4 to correct the finite difference scheme. This correction is intended to eliminate the singularity. Using this factor, the load estimated by CFAT is,

$$\tilde{p}^{\mathrm{CFAT}}(x_i, y_i) = -\rho h \omega^2 \tilde{w}(x_i, y_i) + D\left(\mu^4 \delta_\Delta^{4x}(x_i, y_i) + 2\nu^4 \delta_\Delta^{2x2y}(x_i, y_i) + \mu^4 \delta_\Delta^{4y}(x_i, y_i)\right). \tag{7}$$

The CFAT response is then [15],

$$E^{\mathrm{CFAT}} = \frac{\dfrac{4\mu^4(1-\cos(k_x\Delta))^2 + 4\mu^4(1-\cos(k_y\Delta))^2 + 8\nu^4(1-\cos(k_x\Delta))(1-\cos(k_y\Delta))}{\Delta^4} - k_\mathrm{f}^4}{(k_x^2 + k_y^2)^2 - k_\mathrm{f}^4}. \tag{8}$$

The factor μ^4 is obtained by zeroing the numerator of eq. (6) when $k_x = 0$ and $k_y = k_\mathrm{f}$ [15] :

$$\mu^4 = \frac{\Delta^4 k_\mathrm{f}^4}{(2 - 2\cos(k_\mathrm{f}\Delta))^2}. \tag{9}$$

The factor ν^4 is obtained by zeroing the numerator when $k_x = k_\mathrm{f}/\sqrt{2}$ and $k_y = k_\mathrm{f}/\sqrt{2}$ [15] :

$$\nu^4 = \frac{\Delta^4 k_\mathrm{f}^4}{8\left(1 - \cos\left(\dfrac{k_\mathrm{f}\Delta}{\sqrt{2}}\right)\right)^2} - \mu^4. \tag{10}$$

Note that it is possible to choose other points where the numerator is set to zero. The arbitrary choice presented in this article is the same as in the study presented in [15]. However, other approaches can be chosen, such as the one used in [17], which involves using a least-squares approach to estimate the corrective factors. Finally, FAT and CFAT responses for $n = 4$ and $n = 2.5$ are shown in figure 1. The singularity on the circle of equation $\sqrt{k_x^2 + k_y^2} = k_\mathrm{f}$ is clearly visible on the FAT plots. The effects of the correction are visible on the CFAT plots.
FAT response includes a low-pass wavenumber filter of the transverse displacements. The filter is particularly useful for avoiding aliasing effects. Indeed, Shannon's sampling criterion stipulates that for a given value of n, the wavenumber components k_x and k_y must be such that :

$$\sqrt{k_x^2 + k_y^2}/k_\mathrm{f} < n/2 \tag{11}$$

The magnitude of the response of the method must therefore be low on the circle $\frac{\sqrt{k_x^2+k_y^2}}{k_\mathrm{f}} = \frac{n}{2}$ and beyond. This is the case for FAT thanks to this filter. For example on the $n = 4$ plot, the maximum value of FAT response on the circle $\sqrt{k_x^2 + k_y^2}/k_\mathrm{f} = 2$ (dark dotted circle in figure 1a) is -8 dB. One of the advantages of CFAT is that this low-pass wavenumber filter is retained by the correcting factors. Indeed, on the $n = 4$ graph, the maximum value of the CFAT response on the circle $\sqrt{k_x^2 + k_y^2}/k_\mathrm{f} = 2$ (dark dotted circle in figure 1c) is -6 dB. It is worth noting that, thanks to this low-pass filter, CFAT can be applied to identify either a dynamic load or a bending stiffness down to $n = 1.85$, below the Shannon criterion ($n = 2$) [15].

2.3. FAT and CFAT for equivalent bending stiffness identification

FAT and CFAT can be used to identify the plate equivalent complex bending stiffness $D/(\rho h)$. Considering a position (x, y) where the applied pressure $\tilde{p}(x, y)$ is zero, eq. (1) becomes,

$$\frac{D}{\rho h} = \frac{\omega^2 \tilde{w}(x, y)}{\dfrac{\partial^4 \tilde{w}(x, y)}{\partial x^4} + 2\dfrac{\partial^4 \tilde{w}(x, y)}{\partial x^2 \partial y^2} + \dfrac{\partial^4 \tilde{w}(x, y)}{\partial y^4}}. \tag{12}$$

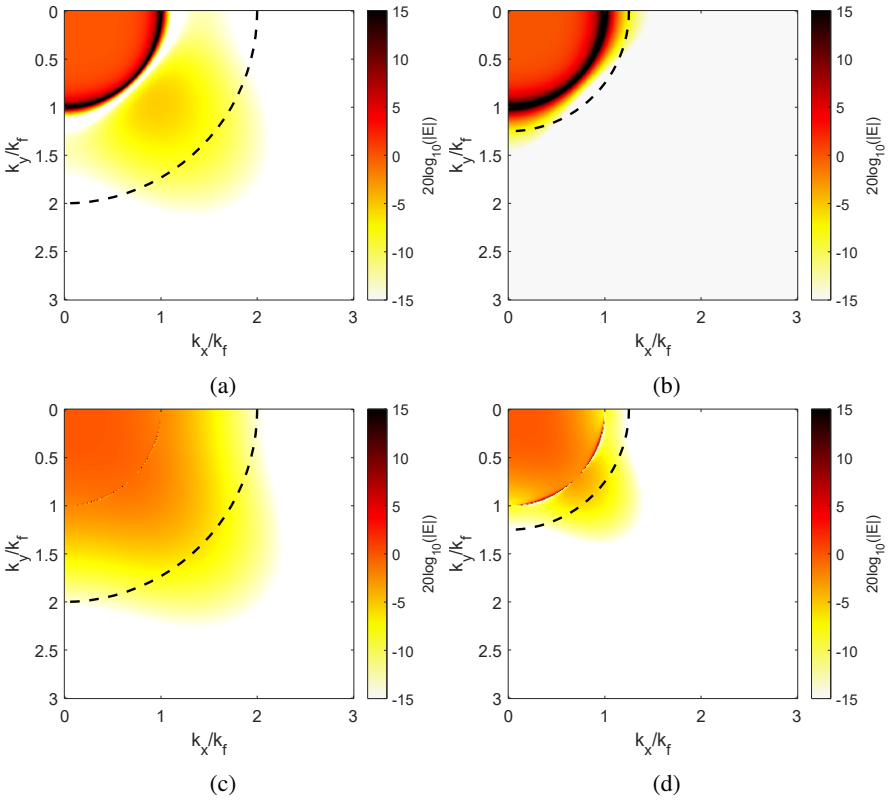

Figure 1: Responses of FAT and CFAT in the wavenumber domain as a function of k_x/k_f and k_y/k_f, (a) FAT response in the wavenumber domain for $n = 4$, (b) FAT response in the wavenumber domain for $n = 2.5$, (c) CFAT response in the wavenumber domain for $n = 4$, (d) CFAT response in the wavenumber domain for $n = 2.5$. The dark dotted circle represents the Nyquist circle $\sqrt{k_x^2 + k_y^2}/k_f = n/2$.

The fourth order spatial derivatives of $\tilde{w}(x, y)$ are again estimated using the same finite difference scheme. The equivalent complex bending stiffness estimated by FAT at point (x_i, y_i) is given by :

$$\left(\frac{D}{\rho h}\right)^{\text{FAT}}_{(x_i,y_i)} = \frac{\omega^2 \tilde{w}(x_i, y_i)}{\delta_\Delta^{4x}(x_i, y_i) + 2\delta_\Delta^{2x2y}(x_i, y_i) + \delta_\Delta^{4y}(x_i, y_i)}. \tag{13}$$

As presented in section 2.2, CFAT corrects the FAT estimate of the fourth-order spatial derivatives by means of two corrective factors μ^4 and ν^4. When FAT is applied to identify an equivalent complex bending stiffness, the bias introduced by the finite difference scheme when n is small is always present. Therefore, to identify this equivalent complex bending stiffness when $n < 4$, the corrective factors are again used to correct the estimate of the fourth-order spatial derivatives :

$$\left(\frac{D}{\rho h}\right)^{\text{CFAT}}_{(x_i,y_i)} = \frac{\omega^2 \tilde{w}(x_i, y_i)}{\mu^4\delta_\Delta^{4x}(x_i, y_i) + 2\nu^4\delta_\Delta^{2x2y}(x_i, y_i) + \mu^4\delta_\Delta^{4y}(x_i, y_i)}. \tag{14}$$

The main advantage of FAT and CFAT is their local aspect. Indeed, when the methods are applied to identify a dynamic load or an equivalent complex bending stiffness at a given point (x_i, y_i) of the plate, the only required information is the displacement field at the 13 points used in the finite difference scheme. In particular, this aspect allows both methods to be applied with any boundary conditions of the plate.

3. Virtual Fields Method for dynamic forces and equivalent bending stiffness identification

The VFM is based on the Principle of Virtual Work (PVW). This principle is a weak form of equilibrium. Consequently, the continuity conditions of the variables involved in the principle are weaker than that required by eq. (1) on which CFAT and FAT are based and which is a strong form [37]. For an isotropic, homogeneous Love-Kirchhoff plate, the PVW is given by [31],

$$\int_{S_v} \tilde{p}(x,y) w^v(x,y) \mathrm{dS} = D \int_{S_v} \left(\tilde{\kappa}_x(x,y) + \tilde{\kappa}_y(x,y)\right)\left(\kappa_x^v(x,y) + \kappa_y^v(x,y)\right) \mathrm{dS} - \rho h \omega^2 \int_{S_v} \tilde{w}(x,y) w^v(x,y) \mathrm{dS}, \quad (15)$$

where $\tilde{\kappa}_x = -\partial^2 \tilde{w}(x,y)/\partial x^2$ and $\tilde{\kappa}_y = -\partial^2 \tilde{w}(x,y)/\partial y^2$ denote bending curvatures along x and y respectively. The terms w^v, $\tilde{\kappa}_x^v$ and $\tilde{\kappa}_y^v$ designate virtual displacement and curvatures, respectively. The VFM consists in choosing the virtual displacement to solve the PVW. When a load or a structural parameter is to identified, the chosen virtual displacement needs to be a kinematically admissible and C^1 function [37]. For example, if a simply supported plate is considered, the transverse displacement is zero at the edges of the structure. Therefore, to be kinematically admissible, the virtual displacement w^v must also be zero at the edges of the structure. Provided they comply with the above conditions, an infinite number of possible virtual fields can be used to solve the Principle of Virtual Work [31]. This freedom is one of the advantages of the VFM. Here, eq (15) is written considering that the virtual displacement is defined as a piecewise function which is zero over the entire surface of the plate, with the exception of a small area called the virtual window S_v. It is an extension of the virtual segment used in [35] in the case of an Euler-Bernoulli beam. The C^1 condition is then satisfied by using a virtual displacement that vanishes at the limit of the integration domain, and whose first-order spatial derivatives also vanish at the limit of the integration domain. Note that D, h and ρ are now and hereafter assumed to be constant over the virtual window. In addition, if the virtual window is small, the external pressure can be assumed constant over S_v. It should be noted that this approach is identical to that adopted by Berry et al. to identify dynamic forces in [31] and [32] and is based on a similar idea to that adopted by Mei et al. in [38] to identify inhomogeneous distributions of elastic properties. In practice, the vibration field of the plate is measured on a regular mesh grid. Then, as shown in figure 2, the virtual window scans the entire surface of the plate and for each of its positions, the PVW is solved and the applied pressure is identified locally.

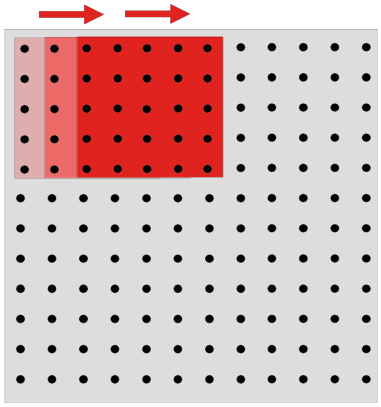

Figure 2: An example of a 5×5 virtual window S_v scanning the plate surface.

3.1. Virtual Fields Method for equivalent bending stiffness identification

The VFM can also be applied to identify the equivalent complex bending stiffness (hereinafter referred to as complex bending stiffness). Assuming that D, ρ and h are constant over S_v and considering a point (x, y) where no external load is applied, the PVW becomes,

$$\left(\frac{D}{\rho h}\right)^{\mathrm{VFM}} = \frac{\omega^2 \int_{S_v} \tilde{w}(x,y) w^v(x,y)\, \mathrm{dS}}{\int_{S_v} \left(\tilde{\kappa}_x(x,y) + \tilde{\kappa}_y(x,y)\right)\left(\kappa_x^v(x,y) + \kappa_y^v(x,y)\right) \mathrm{dS}}. \quad (16)$$

Here, it is the cancellation of the pressure term in eq. (15) that allows the VFM to be applied to identify a complex bending stiffness. The conditions relating to the virtual fields introduced above are unchanged. They must still be any kinematically admissible and C^1 function and the choice of defining them piecewise on a virtual window is retained. The practical implementation of the method remains the same as for force identification. The virtual window scans the surface of the plate and, for each of its positions, the complex bending stiffness is identified locally. The application of the VFM with a virtual window provides a local aspect to the method. Thanks to this local aspect, the VFM can be applied to identify either a dynamic load or a complex bending stiffness at a given position (x_i, y_i) without any knowledge of the displacement field outside the area covered by the virtual window. The principles presented in this section are used in the following section to develop the Frequency-Adapted VFM formalism.

4. Frequency-Adapted Virtual Fields Method

In this section, the frequency adaptation process of the VFM is recalled [35]. As detailed later in the section, this process consists mainly in determining a Frequency-Adapted size for the virtual window S_v.

4.1. Polynomial interpolation of the displacement field

As in the case of the Euler-Bernoulli beam [35], the first step in the frequency adaptation process is to interpolate the displacement field using a polynomial. In [35], the Newton formula was used. Thus, a 2D extension of this formula, Newton's bivariate polynomial interpolation [39], is applied here. Again, as in [35], interpolation of the displacement field enables integrals to be calculated analytically in the PVW (eq. (16)). As highlighted in section 4.3, this calculation is essential for the development of the FA VFM formalism. The $N \times M$ rectangular experimental mesh shown in figure 3 is considered. The transverse displacement is known at each mesh node. The polynomial function that interpolates

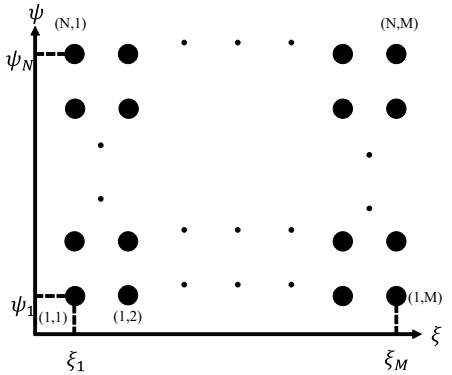

Figure 3: An experimental mesh of size $N \times M$ with local coordinates ξ and ψ

the displacement measured on the mesh is given by [39],

$$W^P(\xi, \psi) = \boldsymbol{\xi}^T \mathbf{P} \boldsymbol{\psi}, \tag{17}$$

where

$$\boldsymbol{\xi} = \begin{pmatrix} 1 \\ \xi - \xi_1 \\ (\xi - \xi_1)(\xi - \xi_2) \\ \vdots \\ (\xi - \xi_1)(\xi - \xi_2)...(\xi - \xi_{N-1}) \end{pmatrix} \quad \text{and} \quad \boldsymbol{\psi} = \begin{pmatrix} 1 \\ \psi - \psi_1 \\ (\psi - \psi_1)(\psi - \psi_2) \\ \vdots \\ (\psi - \psi_1)(\psi - \psi_2)...(\psi - \psi_{N-1}) \end{pmatrix}, \tag{18}$$

are dimensionless coordinates whose expression is given in section 4.2. Assuming that $N \geq M$, the matrix $\mathbf{P}$ is given by [40],

$$\mathbf{P} = \begin{pmatrix} p_{0,0}^{(0)} & p_{0,1}^{(1)} & \cdots & p_{0,M}^{(M)} \\ p_{1,0}^{(1)} & p_{1,1}^{(1)} & \cdots & p_{1,M}^{(M)} \\ \vdots & \vdots & \ddots & \vdots \\ p_{M,0}^{(M)} & p_{M,1}^{(M)} & \cdots & p_{M,M}^{(M)} \\ p_{M+1,0}^{(M+1)} & p_{M+1,1}^{(M+1)} & \cdots & p_{M+1,M}^{(M+1)} \\ \vdots & \vdots & \ddots & \vdots \\ p_{N,0}^{(N)} & p_{N,1}^{(N)} & \cdots & p_{N,M}^{(N)} \end{pmatrix}, \tag{19}$$

with,

$$p_{l,o}^{(i)} = \begin{cases} \dfrac{p_{l,o}^{(i-1)} - p_{l-1,o}^{(i-1)}}{\xi_l - \xi_{l-i}} \text{ if } o < i \text{ and } l \geq i, \\ \dfrac{p_{l,o}^{(i-1)} - p_{l,o-1}^{(i-1)}}{\psi_o - \psi_{o-i}} \text{ if } l < i \text{ and } o \geq i, \\ \dfrac{p_{l,o}^{(i-1)} + p_{l-1,o-1}^{(i-1)} - p_{l-1,o}^{(i-1)} - p_{l,o-1}^{(i-1)}}{(\psi_o - \psi_{o-i})(\xi_l - \xi_{l-i})} \text{ if } l \geq i \text{ and } o \geq i, \\ p_{l,o}^{(i-1)} \text{ if } l < i \text{ and } o < i, \\ p_{l,o}^{(0)} = \tilde{w}_{l+1,o+1}, \end{cases} \tag{20}$$

where $\tilde{w}_{l+1,o+1}$ denotes the measured displacement at node $(l+1, o+1)$ in figure 3.

4.2. Virtual Fields Method for $M = 5$ and $N = 5$

The case where $M = N = 5$ is now considered. These values of M and N are chosen to be consistent with the 13-points finite difference scheme used in FAT and CFAT. The displacement interpolation zone is a subset of the measurement mesh centered at point i with coordinates (x_i, y_i). This zone is illustrated in figure 4. Newton's formula described in section 4.1 is applied for $\xi \in [-2, 2]$, and $\psi \in [-2, 2]$ as shown on figure 4b

$$\tilde{w}(x,y) \simeq W^P(\xi,\psi) = \begin{pmatrix} 1 \\ \xi+2 \\ (\xi+2)(\xi+1) \\ \xi(\xi+2)(\xi+1) \\ (\xi-1)\xi(\xi+2)(\xi+1) \end{pmatrix}^T \begin{pmatrix} P_{1,1} & P_{2,1} & P_{3,1} & P_{4,1} & P_{5,1} \\ P_{1,2} & P_{2,2} & P_{3,2} & P_{4,2} & P_{5,2} \\ P_{1,3} & P_{2,3} & P_{3,3} & P_{4,3} & P_{5,3} \\ P_{1,4} & P_{2,4} & P_{3,4} & P_{4,4} & P_{5,4} \\ P_{1,5} & P_{2,5} & P_{3,5} & P_{4,5} & P_{5,5} \end{pmatrix} \begin{pmatrix} 1 \\ \psi+2 \\ (\psi+2)(\psi+1) \\ \psi(\psi+2)(\psi+1) \\ (\psi-1)\psi(\psi+2)(\psi+1) \end{pmatrix}, \tag{21}$$

where here $\xi = \frac{x-x_i}{\Delta}$ and $\psi = \frac{y-y_i}{\Delta}$. The elements of the $\mathbf{P}$ matrix are detailed in Appendix A. The polynomial interpolations of the curvatures $\tilde{\kappa}_x$ and $\tilde{\kappa}_y$ are obtained by a second-order derivation of eq. (21) :

$$\tilde{\kappa}_x \simeq K_x^P = -\frac{1}{\Delta^2}\frac{\partial^2 W^P(\xi,\psi)}{\partial \xi^2} \text{ and } \tilde{\kappa}_y \simeq K_y^P = -\frac{1}{\Delta^2}\frac{\partial^2 W^P(\xi,\psi)}{\partial \psi^2}. \tag{22}$$

The VFM is applied with a square virtual window $S_v = [-\tau, \tau] \times [-\tau, \tau]$, where $\tau \leq 2.5$, as shown in figure 4b. The $\tau \leq 2.5$ limit is set to strictly cover the 5×5 points used in the interpolation of measured displacements and

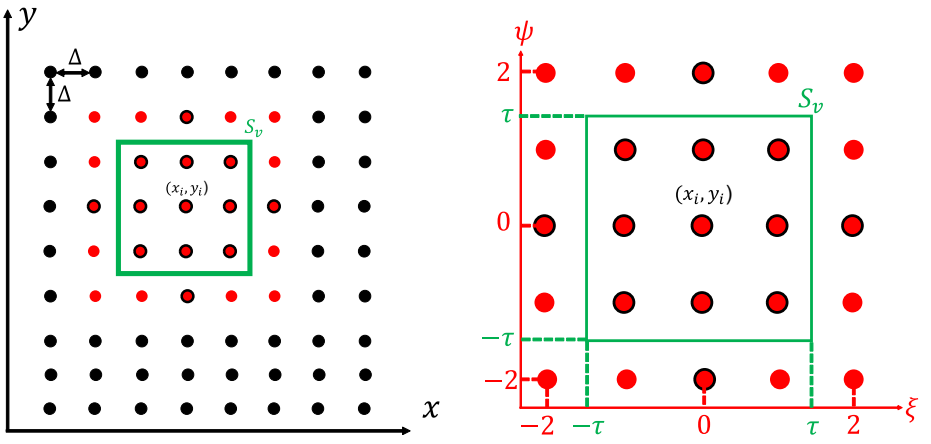

Figure 4: Schematic of the interpolation zone for $N = M = 5$, (a) The experimental mesh with: in red the points used in the interpolation of the displacement field and in green the virtual window. The red points circled in black are those used in the finite difference scheme involved in FAT and CFAT, (b) Local coordinates over the interpolation area.

thus avoid extrapolation. Note that the value of τ is the quantity that will be adapted as a function of frequency. This window is divided into four quadrants, as shown in figure 5 [31]. The virtual displacement here is based on Hermite16

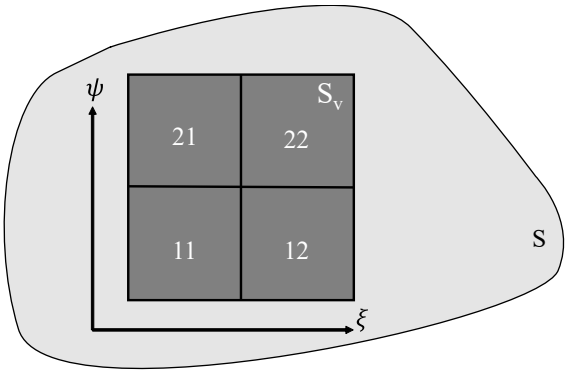

Figure 5: Virtual window S_v divided into four quadrants placed over a plate of surface S,

interpolation functions that respect the conditions detailed in section 3 [37, 31]. The virtual displacement is defined over each quadrant separately [31] :

$$
\begin{aligned}
w^v(\xi,\psi) &= H_2\left(\frac{2\xi}{\tau}+1\right) H_2\left(\frac{2\psi}{\tau}+1\right) \text{ for } \xi \in [-\tau, 0] \text{ and } \psi \in [-\tau, 0], \text{ on quadrant 11,} \\
w^v(\xi,\psi) &= H_1\left(\frac{2\xi}{\tau}-1\right) H_2\left(\frac{2\psi}{\tau}+1\right) \text{ for } \xi \in [0, \tau] \text{ and } \psi \in [-\tau, 0], \text{ on quadrant 12,} \\
w^v(\xi,\psi) &= H_2\left(\frac{2\xi}{\tau}+1\right) H_1\left(\frac{2\psi}{\tau}-1\right) \text{ for } \xi \in [-\tau, 0] \text{ and } \psi \in [0, \tau], \text{ on quadrant 21,} \\
w^v(\xi,\psi) &= H_1\left(\frac{2\xi}{\tau}-1\right) H_1\left(\frac{2\psi}{\tau}-1\right) \text{ for } \xi \in [0, \tau] \text{ and } \psi \in [0, \tau], \text{ on quadrant 22,}
\end{aligned}
\tag{23}
$$

where $H_1(\xi') = \frac{1}{4}\left(2+\xi'\right)\left(1-\xi'\right)^2$ and $H_2(\xi') = \frac{1}{4}\left(2-\xi'\right)\left(1+\xi'\right)^2$. The virtual curvatures are then calculated on each quadrant using :

$$\begin{aligned}\kappa_x^v(x,y) &= -\frac{\partial^2 w^v(x,y)}{\partial x^2}\\ \kappa_y^v(x,y) &= -\frac{\partial^2 w^v(x,y)}{\partial y^2}\end{aligned} \tag{24}$$

The virtual displacement and virtual curvatures are shown in figure 6. The VFM is applied using eqs. (21), (23) and

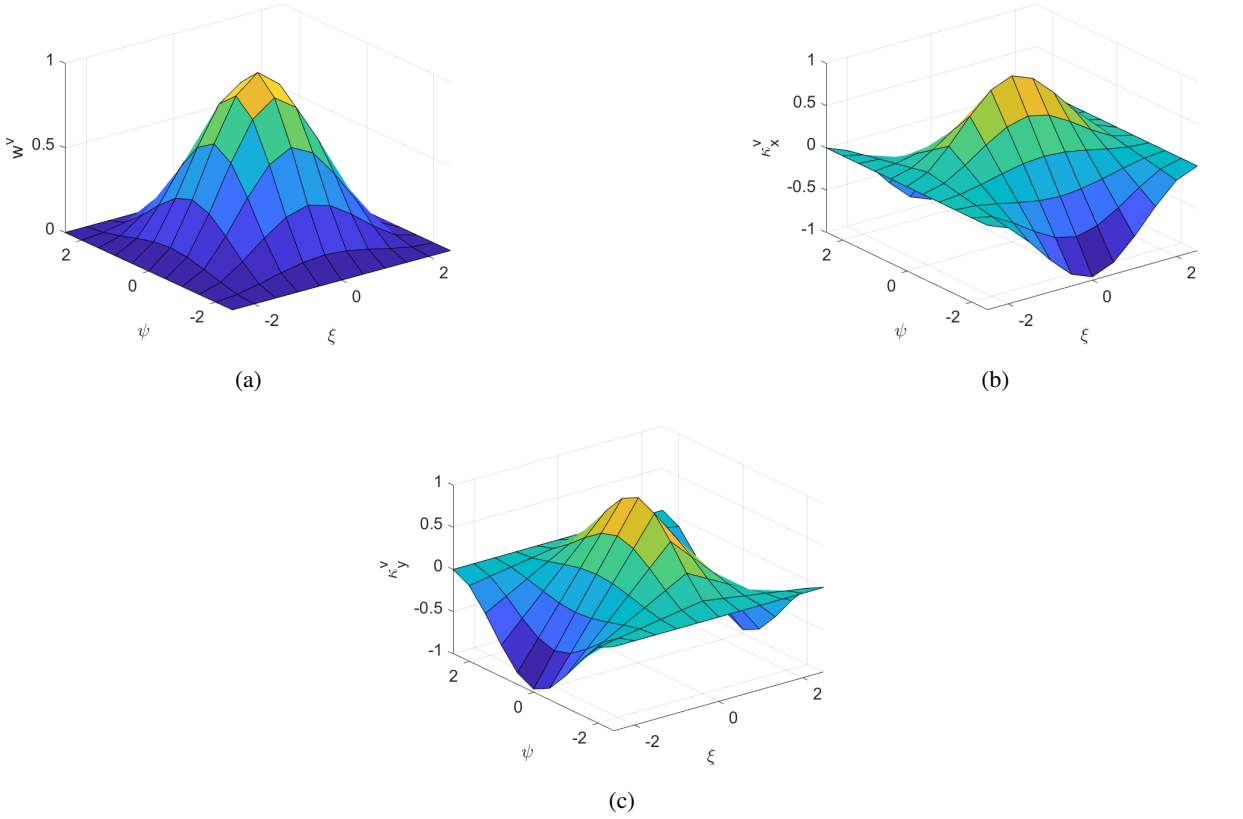

(a) (b) (c)

Figure 6: Virtual fields for $\tau = 2.5$, (a) Virtual displacement w^v, (b) Virtual curvature κ_x^v, (c) Virtual curvature κ_y^v.

(24) to identify the applied pressure at point i :

$$\begin{aligned}\tilde{p}^{\mathrm{VFM}}(x_i,y_i)\int_{-\tau}^{\tau}\int_{-\tau}^{\tau} w^v(\xi,\psi)\mathrm{d}\xi\mathrm{d}\psi = D\int_{-\tau}^{\tau}\int_{-\tau}^{\tau}\left(K_x^P(\xi,\psi)+K_y^P(\xi,\psi)\right)\left(\kappa_x^v(\xi,\psi)+\kappa_y^v(\xi,\psi)\right)\mathrm{d}\xi\mathrm{d}\psi\\ -\rho h\omega^2\int_{-\tau}^{\tau}\int_{-\tau}^{\tau} W^P(\xi,\psi)w^v(\xi,\psi)\mathrm{d}\xi\mathrm{d}\psi.\end{aligned} \tag{25}$$

Here, the term $\tilde{p}^{\mathrm{VFM}}$ is the averaged pressure on the virtual window. Note that the integration on the left-hand side of eq. (25) acts like a low-pass wavenumber filter. The integrals of eq. (25) can be calculated exactly since the integrands are polynomials. The pressure is then,

$$\begin{aligned}\tilde{p}^{\mathrm{VFM}}(x_i,y_i) = \frac{D}{\Delta^4}\left(B_0\gamma^{00}_{(x_i,y_i)} + B_1\gamma^{11}_{(x_i,y_i)} + B_2\gamma^{22}_{(x_i,y_i)} + B_3\gamma^{21}_{(x_i,y_i)} + B_4\gamma^{20}_{(x_i,y_i)} + B_5\gamma^{10}_{(x_i,y_i)}\right)\\ -\rho h\omega^2\left(A_0\gamma^{00}_{(x_i,y_i)} + A_1\gamma^{11}_{(x_i,y_i)} + A_2\gamma^{22}_{(x_i,y_i)} + A_3\gamma^{21}_{(x_i,y_i)} + A_4\gamma^{20}_{(x_i,y_i)} + A_5\gamma^{10}_{(x_i,y_i)}\right),\end{aligned} \tag{26}$$

with

$$\gamma^{00}_{(x_i,y_i)} = \tilde{w}_{0,0}, \quad \gamma^{11}_{(x_i,y_i)} = \tilde{w}_{1,-1} + \tilde{w}_{-1,1} + \tilde{w}_{-1,-1} + \tilde{w}_{1,1}, \quad \gamma^{22}_{(x_i,y_i)} = \tilde{w}_{-2,2} + \tilde{w}_{2,-2} + \tilde{w}_{-2,-2} + \tilde{w}_{2,2},$$
$$\gamma^{21}_{(x_i,y_i)} = \tilde{w}_{-1,2} + \tilde{w}_{1,2} + \tilde{w}_{-2,1} + \tilde{w}_{2,1} + \tilde{w}_{1,-2} + \tilde{w}_{2,-1} + \tilde{w}_{-2,-1} + \tilde{w}_{-1,-2}, \tag{27}$$
$$\gamma^{20}_{(x_i,y_i)} = \tilde{w}_{0,2} + \tilde{w}_{-2,0} + \tilde{w}_{0,-2} + \tilde{w}_{2,0}, \quad \gamma^{10}_{(x_i,y_i)} = \tilde{w}_{0,1} + \tilde{w}_{-1,0} + \tilde{w}_{0,-1} + \tilde{w}_{1,0},$$

where $\tilde{w}_{o,l} = \tilde{w}(x_i + o\Delta, y_i + l\Delta)$. The coefficients A_i and B_i are polynomial functions of τ, that are detailed in appendix B.

4.3. Wavenumber analysis

Thanks to the polynomial interpolation described in section 4.1, eq. (26) provides an expression for $\tilde{p}^{\mathrm{VFM}}$ as a linear combination of the values of the displacement measured at each node of the 5×5 mesh. In order to find the Frequency-Adapted value of τ, the Fourier transform of eq. (26) is computed,

$$\begin{aligned}\hat{p}^{\mathrm{VFM}}(k_x, k_y) = \frac{D}{\Delta^4}\Big[&B_0 + 4B_1C_xC_y + 4B_2(2C_x^2 - 1)(2C_y^2 - 1) + 4B_3(2C_xC_y^2 + 2C_x^2C_y - C_x - C_y) + \\ &4B_4(C_x^2 + C_y^2 - 1) + 2B_5(C_x + C_y)\Big] - \rho h\omega^2\Big[A_0 + 4A_1C_xC_y + 4A_2(2C_x^2 - 1)(2C_y^2 - 1) + \\ &4A_3(2C_xC_y^2 + 2C_x^2C_y - C_x - C_y) + 4A_4(C_x^2 + C_y^2 - 1) + 2A_5(C_x + C_y)\Big],\end{aligned} \tag{28}$$

with $C_x = \cos(k_x\Delta)$ and $C_y = \cos(k_y\Delta)$. The VFM response is then given by,

$$\begin{aligned}E^{\mathrm{VFM}} = \frac{\hat{p}^{\mathrm{VFM}}}{\hat{p}} = &\frac{1}{(k_x^2 + k_y^2)^2 - k_{\mathrm{f}}^4} \times \Big[\frac{1}{\Delta^4}\Big(B_0 + 4B_1C_xC_y + 4B_2(2C_x^2 - 1)(2C_y^2 - 1) + \\ &4B_3(2C_xC_y^2 + 2C_x^2C_y - C_x - C_y) + 4B_4(C_x^2 + C_y^2 - 1) + 2B_5(C_x + C_y)\Big) - k_{\mathrm{f}}^4\Big(A_0 + \\ &4A_1C_xC_y + 4A_2(2C_x^2 - 1)(2C_y^2 - 1) + 4A_3(2C_xC_y^2 + 2C_x^2C_y - C_x - C_y) + \\ &4A_4(C_x^2 + C_y^2 - 1) + 2A_5(C_x + C_y)\Big)\Big].\end{aligned} \tag{29}$$

It should be noted that the calculation of this response is essential for finding the Frequency-Adapted value of τ. It turns out that, without interpolation, the expression for the pressure given by eq. (26) would not have been obtained and therefore the calculation of the response introduced eq. (29) would not have been possible. The VFM response again shows a singularity on the circle $\sqrt{k_x^2 + k_y^2} = k_{\mathrm{f}}$. With CFAT the singularity is corrected using the coefficients μ^4 and ν^4. The VFM can be Frequency-Adapted by choosing the value of the half-length of the virtual window, τ, which will make the numerator of eq. (29) be zero on a point of the circle $\sqrt{k_x^2 + k_y^2} = k_{\mathrm{f}}$. The point $k_x = k_{\mathrm{f}}$, $k_y = 0$ is considered. This Frequency-Adapted value of τ therefore has to satisfy the equation :

$$\begin{aligned}&\left(\frac{n}{2\pi}\right)^4\left[\left(8B_2 + 8B_3 + 4B_4\right)\cos\left(\frac{2\pi}{n}\right)^2 + \left(4B_1 + 4B_3 + 2B_5\right)\cos\left(\frac{2\pi}{n}\right) + B_0 - 4B_2 - 4B_3 + 2B_5\right] - \\ &\left(8A_2 + 8A_3 + 4A_4\right)\cos\left(\frac{2\pi}{n}\right)^2 + \left(4A_1 + 4A_3 + 2A_5\right)\cos\left(\frac{2\pi}{n}\right) + A_0 - 4A_2 - 4A_3 + 2A_5 = 0,\end{aligned} \tag{30}$$

where the coefficients A_i, B_i, which depend on τ are detailed in appendix B. The solution of eq. (30) is obtained using the Matlab® *symbolic toolbox*. Four solutions are obtained, but only one lies in the interval $[0, 2.5]$ as long as $n > 2$, which is the Nyquist limit. Only this solution is therefore compatible with the problem. It corresponds to the Frequency-Adapted value of the half-length of the virtual window τ_{FA} :

$$\tau^0_{\mathrm{FA}} = \frac{\sqrt{14\,\pi^2\sin\left(\frac{\pi}{n}\right)^2 - 9\sqrt{35\,n^4\sin\left(\frac{\pi}{n}\right)^4 + \frac{196\,\pi^4\sin\left(\frac{\pi}{n}\right)^4}{81} + \frac{392\,\pi^4\sin\left(\frac{\pi}{n}\right)^2}{27} - \frac{119\,\pi^4}{9}} + 42\,\pi^2}}{3\pi\left|\sin\left(\frac{\pi}{n}\right)\right|}. \tag{31}$$

Frequency adaptation of the virtual window size can be performed using any point on the circle of equation $\sqrt{k_x^2 + k_y^2} = k_\mathrm{f}$ for which the numerator of eq. (29) is null. Each point on the first quarter-circle will give a different value for the Frequency-Adapted window side length. Figure 7 shows the evolution of τ_{FA}^0 as a function of n (eq. (31)). The Frequency-Adapted values of τ obtained using the points $\left(k_\mathrm{f}/\sqrt{2}, k_\mathrm{f}/\sqrt{2}\right)$ and $\left(k_\mathrm{f}/2, \sqrt{3}k_\mathrm{f}/2\right)$ are also shown. Note that the value of τ_{FA}^0 is the same as the Frequency-Adapted value of the virtual segment found in the 1D case

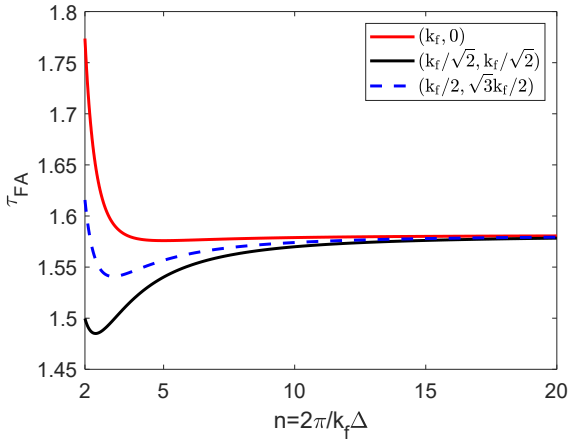

Figure 7: Frequency-Adapted value of the half length of the virtual window in the VFM as a function of $n \in [2, 20]$ and for various points on the circle $\sqrt{k_x^2 + k_y^2} = k_\mathrm{f}$. In red $\tau = \tau_{\mathrm{FA}}^0 : (k_\mathrm{f}, 0)$, in black $\tau = \tau_{\mathrm{FA}}^{\pi/4} : \left(k_\mathrm{f}/\sqrt{2}, k_\mathrm{f}/\sqrt{2}\right)$ and in dotted blue $\tau = \tau_{\mathrm{FA}}^{\pi/3} : \left(k_\mathrm{f}/2, \sqrt{3}k_\mathrm{f}/2\right)$

[35]. With the exception of strong variations at low values of n, τ_{FA}^0, $\tau_{\mathrm{FA}}^{\pi/4}$ and $\tau_{\mathrm{FA}}^{\pi/3}$ are almost constant with n and therefore with frequency. Also, 9 of the 13 points used in the FAT and CFAT finite difference schemes are covered by the Frequency-Adapted virtual window. The VFM response for $\tau = 0.5$ in the wavenumber domain is shown in figure 8 for $n = 4$ and $n = 2.5$. The figure also shows the responses obtained with the Frequency-Adapted VFM using $\tau = \tau_{\mathrm{FA}}^0$. When $\tau = 0.5$ the singularity is clearly visible on the circle $\sqrt{k_x^2 + k_y^2} = k_\mathrm{f}$ for both values of n. The Frequency-Adapted VFM eliminates it satisfactorily. However, it remains more present than in CFAT (see figures 1c and 1d), particularly for $n = 2.5$ (figure 8d). This is due to the fact that CFAT uses two correction factors and therefore corrects the response at two points $(k_\mathrm{f}, 0)$ and $\left(k_\mathrm{f}/\sqrt{2}, k_\mathrm{f}/\sqrt{2}\right)$, whereas the VFM is Frequency-Adapted using a single point. Figures 8c and 8d also show that using of τ_{FA}^0 suppresses the singularity at both points $(k_\mathrm{f}, 0)$ and $(0, k_\mathrm{f})$. This is because $E^{\mathrm{VFM}}(0, k_\mathrm{f}) = E^{\mathrm{VFM}}(k_\mathrm{f}, 0)$. Figure 9 shows the Frequency-Adapted VFM responses using $\tau = \tau_{\mathrm{FA}}^{\pi/3}$ and $\tau = \tau_{\mathrm{FA}}^{\pi/4}$ for $n = 2.5$ (the subscripts $\pi/3$ and $\pi/4$ indicate the angular direction on the circle chosen to eliminate the singularity). The choice of this angular direction clearly influences the frequency adaptation. The singularity is always eliminated at the chosen point. However, the removal of the singularity on the rest of the circle depends on the choice of this direction. The singularity is not well suppressed for $\tau = \tau_{\mathrm{FA}}^{\pi/4}$ and even less so for $\tau = \tau_{\mathrm{FA}}^{\pi/3}$. Frequency adaptation using τ_{FA}^0 will be used next. Like FAT, the VFM response for $\tau = 0.5$ presents a low-pass wavenumber filter, and like CFAT, the Frequency-Adapted VFM always preserves this low-pass wavenumber filter.

4.4. Identification of the complex bending stiffness with the Frequency-Adapted VFM

Considering a position (x_i, y_i) where no external load is applied, eq. (26) can be used to identify the complex bending stiffness :

$$\left(\frac{D}{\rho h}\right)^{\mathrm{VFM}}_{(x_i,y_i)} = \frac{\omega^2\left(A_0\gamma^{00}_{(x_i,y_i)} + A_1\gamma^{11}_{(x_i,y_i)} + A_2\gamma^{22}_{(x_i,y_i)} + A_3\gamma^{21}_{(x_i,y_i)} + A_4\gamma^{20}_{(x_i,y_i)} + A_5\gamma^{10}_{(x_i,y_i)}\right)}{\frac{1}{\Delta^4}\left(B_0\gamma^{00}_{(x_i,y_i)} + B_1\gamma^{11}_{(x_i,y_i)} + B_2\gamma^{22}_{(x_i,y_i)} + B_3\gamma^{21}_{(x_i,y_i)} + B_4\gamma^{20}_{(x_i,y_i)} + B_5\gamma^{10}_{(x_i,y_i)}\right)}. \tag{32}$$

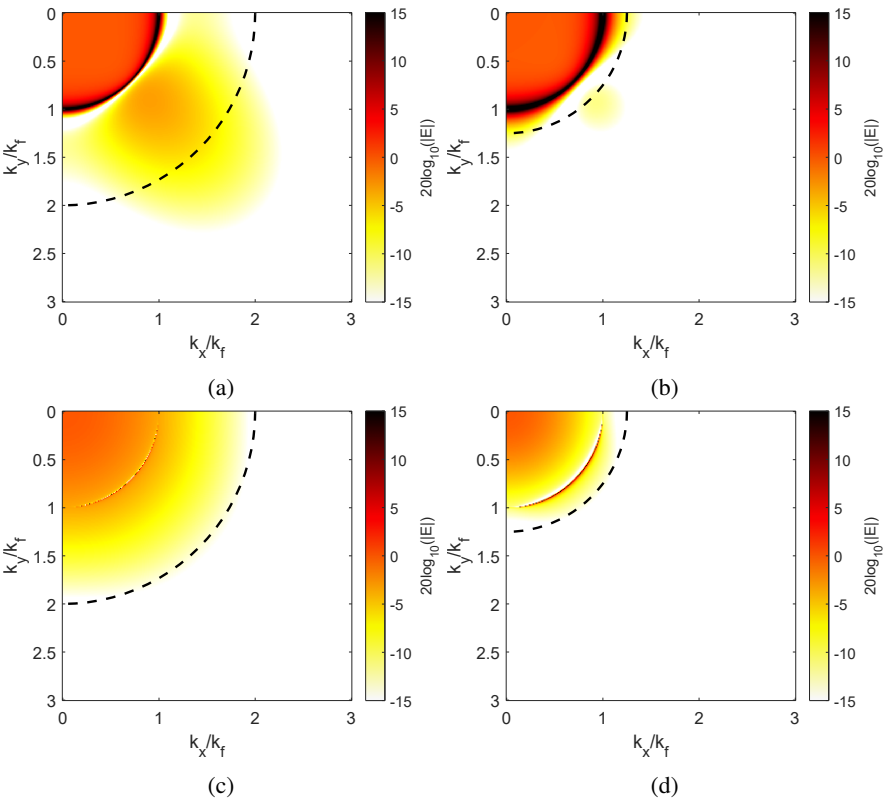

Figure 8: Responses of the VFM for $\tau = 0.5$ and of the Frequency-Adapted VFM as a function of k_x/k_f and k_y/k_f, (a) VFM response for $\tau = 0.5$ in the wavenumber domain for $n = 4$, (b) VFM response for $\tau = 0.5$ in the wavenumber domain for $n = 2.5$, (c) Frequency-Adapted VFM response using $\tau = \tau^0_{\mathrm{FA}}$ in the wavenumber domain for $n = 4$, (d) Frequency-Adapted VFM response using $\tau = \tau^0_{\mathrm{FA}}$ in the wavenumber domain for $n = 2.5$. The dark dotted circle represents the Nyquist circle $\sqrt{k_x^2 + k_y^2}/k_\mathrm{f} = n/2$.

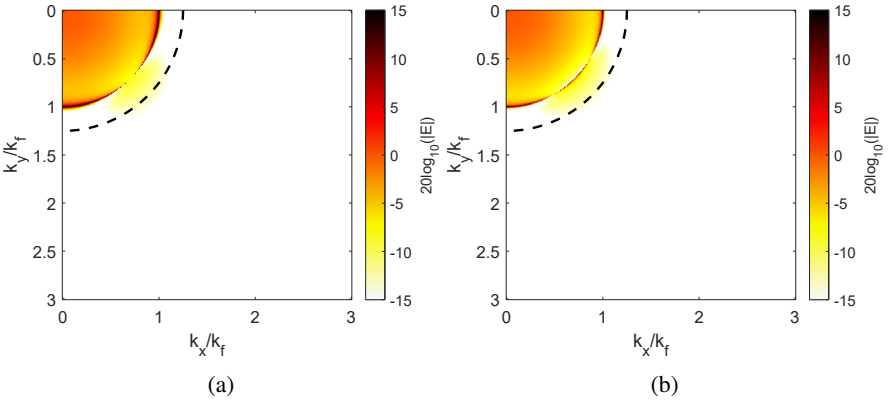

Figure 9: Responses of the Frequency-Adapted VFM in the wavenumber domain as a function of k_x/k_f and k_y/k_f for $n = 2.5$ using different values of τ^{FA}, (a) Using $\tau = \tau^{\mathrm{FA}}_{\pi/4}$, (b) Using $\tau = \tau^{\mathrm{FA}}_{\pi/3}$. The dark dotted circle represents the Nyquist circle $\sqrt{k_x^2 + k_y^2}/k_\mathrm{f} = n/2$.

As seen in section 4.3, the Frequency-Adapted VFM consists in determining a Frequency-Adapted value for the virtual window length. Once done, the method can be applied to identify a dynamic force or complex bending stiffness. This

Frequency-Adapted length is determined using eq. (31). This equation uses the number of measurement points per wavelength $n = 2\pi/k_f\Delta$ which is a function of k_f and therefore of the complex bending stiffness. The parameter n is known in a force identification problem, since the material is known *a priori*. However, this is not the case when it comes to identifying a complex bending stiffness. For 2D structures CFAT faces the same problem [16]. So, like CFAT, an iterative process is used to solve this problem. The VFM is applied with a given virtual window. A first value of $D/(\rho h)$ is then obtained using eq. (32) and so k_f can be determined, from which n is known and the Frequency-Adapted VFM can be used to choose the adapted virtual window size. To refine the estimated value, the process is applied 10 times. This number of iterations was determined empirically, based on the observation that after 10 iterations, the estimated bending stiffness values no longer varied. This iterative process always converges and does not depend on the initial value of the virtual window size.

5. Numerical study for complex bending stiffness identification

5.1. Simulated plate

In order to demonstrate the efficiency of the FA VFM, a numerical study was carried out to identify the complex bending stiffness of an isotropic, homogeneous and infinite Love-Kirchhoff plate. The simulation was performed on a 0.39×0.58 m^2 portion of an infinite Love-Kirchhoff plate. The plate is subjected to a harmonic load. The displacement is simulated at each frequency using the following Green's function [8] :

$$\tilde{w}(x - x_0, y - y_0) = \frac{1}{8k_f^2 D}(H_0^{(1)}(k_f r) - H_0^{(1)}(jk_f r)). \tag{33}$$

Here, x_0 and y_0 represent the coordinates of the point force. The origin of the coordinate system is the bottom left-hand corner of the simulated portion of the plate. The parameter $r = \sqrt{(x - x_0)^2 + (y - y_0)^2}$ is the distance from a point of coordinates (x, y) to the source and $H_0^{(1)}$ is the cylindrical Hankel function of the first type of order 0. Note that here, the panel response consists of a propagative wave emitted at the excitation point and is therefore quite distinct to the low-frequency, modal response of a lightly-damped, finite-dimension plate. However, this situation is closer to the experimental configuration reported in section 6 and should apply to the high-frequency range concerned by the FA VFM approach.

The simulation parameters are chosen to be consistent with the damped case of the experimental study presented in section 6. The frequency range investigated is $[100, 6400]$ Hz. Moreover, in the experimental study, a rope is passed through successive holes along a third of the plate's contour. The bending waves are therefore attenuated at the edges of the structure. This aspect of the experimental set-up justifies an infinite plate model in this numerical study. The source coordinates are $x_0 = 0.11$ m and $y_0 = 0.17$ m. The Young's modulus is considered to be complex to take account of structural dissipation: $\tilde{E} = E(1 + j\eta)$, where η is the structural loss factor. In the experimental study, the plate is locally damped using a foam glued to the plate. It is assumed that the foam adds no stiffness to the plate. The simulations are carried out using the parameter corresponding to the locally damped zone of the plate. The complex bending stiffness normalised by the mass per unit area to be identified is $(D/\mu)^{\text{with Damp.}} = 2.14$ m^4/s^2. Since foam is supposed to considerably increase structural dissipation, the loss factor in the simulation is $\eta = 0.35$. The mesh in this study is made up of 28×41 points with a spacing of 14.5 mm. The flexural wavelength (which depends on D and μ) is supposed to be known a priori, therefore the number of measurement points per flexural wavelength is supposed to be known as well. It varies from 21.1 (at $f = 100$ Hz) to 2.5 (at $f = 6400$ Hz).

5.2. Frequency least squares results

First, CFAT and the FA VFM are applied with the frequency least squares to obtain a map of the identified bending stiffness and loss factor. The objective of the frequency least squares is to obtain a spatial mapping of frequency-averaged (in the least squares sense) values of D/μ. The complex bending stiffness identified at each point (x, y) of the mesh is given by :

$$\left(\frac{D}{\mu}\right)_{(x,y)} = \frac{\mathbf{B}_\omega^H \mathbf{N}_\omega}{\mathbf{B}_\omega^H \mathbf{B}_\omega}, \tag{34}$$

The elements of the column vector $\mathbf{B}_\omega$ correspond to the estimate of the denominator of eq. (32) with the term ω^2 for the VFM (eq. (14) for CFAT) for each frequency at the point where D/μ is identified. Similarly, the elements

of the column vector $\mathbf{N}_\omega$ correspond to the estimate of the numerator of eq. (32) for VFM (eq. (14) for CFAT) for each frequency at the point of identification. Here, as the number of points per bending wavelength is known, the Frequency-Adapted length of the virtual window and the CFAT correction factors can be directly calculated using eqs. (31), (9) and (10) respectively. The identified bending stiffness is the real part of the complex bending stiffness calculated with the two methods, while the loss factor is the ratio between the imaginary part and the real part of the identified complex bending stiffness :

$$\eta = \frac{\mathrm{Im}(D/\mu)}{\mathrm{Re}(D/\mu)}. \tag{35}$$

Frequency least squares are applied using 1001 frequency points in the interval [1000, 5000] Hz. The results are shown in figure 10. The bending stiffness identified with CFAT and the FA VFM is consistent with the simulated value (figures

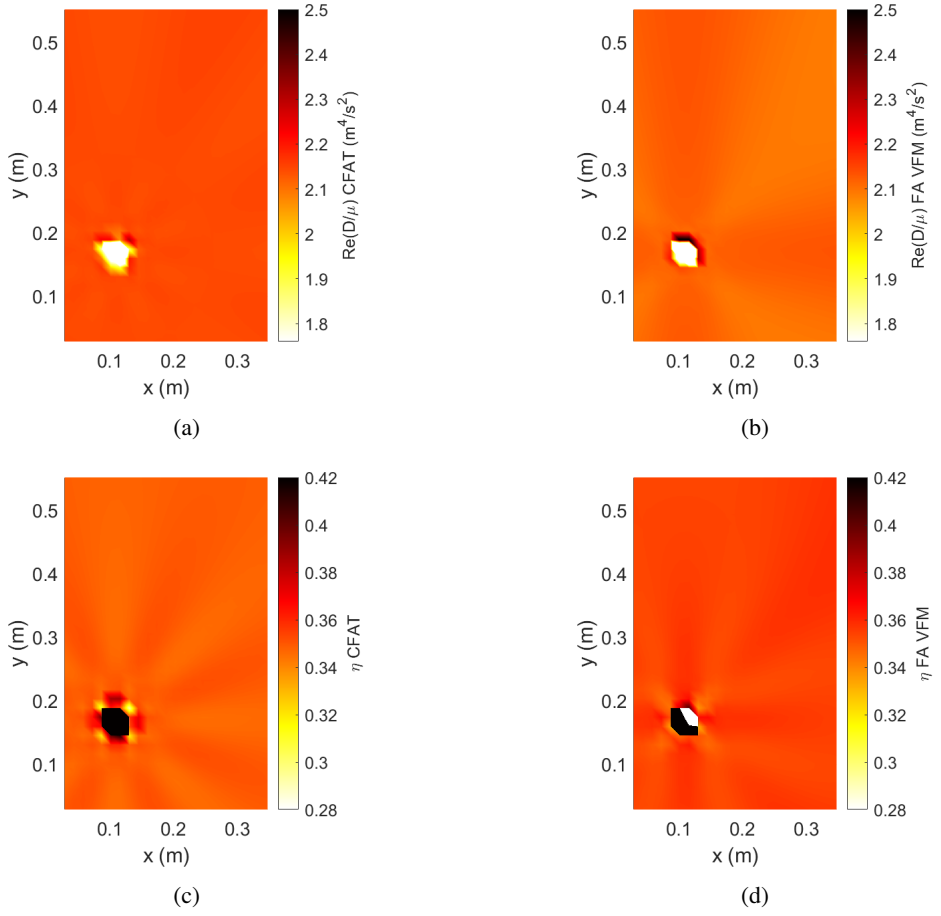

Figure 10: Bending stiffness and loss factor identified with CFAT and the Frequency-Adapted VFM using frequency least squares over the frequency range [1000, 5000] Hz and simulated data, (a) Real part of the complex bending stiffness identified with CFAT, (b) Real part of the complex bending stiffness identified with the Frequency-Adapted VFM, (c) Loss factor (ratio between the imaginary part and real part) identified with CFAT, (d) Loss factor identified with the Frequency-Adapted VFM.

10a and 10b). A disturbance in the maps is observed at the coordinates of the point force. These perturbations are created by the fact that the zero external force assumption on which CFAT and the FA VFM are based is no longer respected at the position of the point force, which leads to an erroneous identification of the complex bending stiffness. The results of CFAT and the FA VFM are similar. With regard to the loss factor (figures 10c and 10d), the results obtained with the methods are consistent with the expected value of 0.35. The loss factor identified at the position of the point force

is again erroneous. Overall, these results show that the FA VFM can be used to map complex bending stiffness. The similarities between the results of the FA VFM and those of CFAT validate the development of the method.

5.3. Spatial least squares results

The frequency least squares approach is used to obtain a spatial identification of the complex bending stiffness. In order to obtain a frequency-dependent identification, spatial least squares are applied. The objective of the spatial least squares is to obtain the frequency dependence of spatially-averaged (in the least squares sense) values of D/μ. The complex bending stiffness estimated at ω using spatial least squares is given by :

$$\left(\frac{D}{\mu}\right)_{\omega} = \omega^2 \frac{\mathbf{B}^H \mathbf{N}}{\mathbf{B}^H \mathbf{B}}, \tag{36}$$

where $\mathbf{B}$ and $\mathbf{N}$ are column vectors. At frequency ω, each element of $\mathbf{B}$ corresponds to the estimate at ω of the denominator of eq. (32) at a measurement point. The elements of $\mathbf{N}$ are obtained in the same way but using the numerator of eq. (32) without the term ω^2. The measurement points used to estimate $\mathbf{B}$ and $\mathbf{N}$ are located in a zone where no external load is applied. The number of points used in the application of the spatial least squares is 449. The results obtained are shown figure 11. The bending stiffness identified using the methods and spatial least squares is

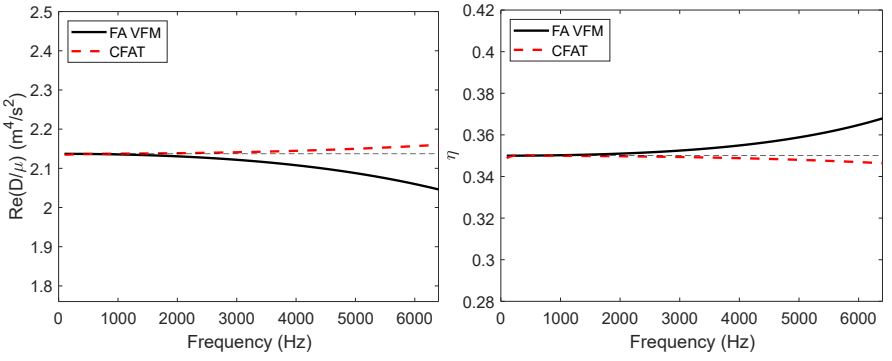

(a) (b)

Figure 11: Bending stiffness and loss factor identified with the Frequency-Adapted VFM and CFAT using spatial least squares and simulated data, (a) Bending stiffness, (b) Loss factor. For each plot, the horizontal dotted black line represents the reference value.

consistent with the expected values over the entire frequency range (figure 11a). It is important to note that CFAT and the FA VFM results differ at high frequencies. Indeed, the bending stiffness identified with the FA VFM above 4000 Hz is slightly underestimated compared to the reference and CFAT results. This result can be explained by the fact that the singularity present in the response of the VFM in the wavenumber domain (figure 8) is less suppressed than in the case of CFAT (figure 1). With regard to the loss factor (figure 11b), the same conclusions can be drawn from the results. The results of the methods are consistent with the expected values. However, the FA VFM slightly overestimates it. As η is given here by the ratio between the imaginary part and the real part of the identified complex bending stiffness, this result is consistent with the underestimation of the real part of the bending stiffness by the FA VFM observed in figure 11a. Indeed, the imaginary part of the complex bending stiffness identified by CFAT is similar to that identified by the FA VFM over the whole frequency range, which shows that the overestimation of the loss factor by the FA VFM observed in figure 11b is indeed linked to the underestimation of the bending stiffness. The results of these simulations demonstrate that the FA VFM can be used to identify the complex bending stiffness of a damped panel over a wide range of frequencies. In the next section, the method will be applied to estimate the complex bending stiffness using experimental data.

6. Experimental study for complex bending stiffness identification

6.1. Experimental set-up

The experimental study is based on measurements carried out and used in [16]. The measurements were performed on a 0.51×0.71 m^2 rectangular panel of thickness $h = 0.965$ mm with free-free boundary conditions. The thickness

of the plate has been accurately measured via its surface area and weight. The panel is made of aluminum ($\rho = 2700$ kg/m^3, Poisson's ratio of 0.35 and $E = 69$ GPa). Young's modulus is still considered complex to take account structural dissipation $\tilde{E} = E(1 + j\eta)$, where η is the structural loss factor. Therefore, in the following results, the structural loss factor is once again extracted from the imaginary part of the complex bending stiffness. As mentioned in section 5.1, a third of the contour of the plate was covered with a rope passed through successive holes to limit the reverberation time of the structure, in order to maintain reasonable measurement times. This configuration is used to show that the methods can be applied with any boundary conditions. A damping zone was created by adding a 15×15 cm^2 square of foam which was glued to the panel. The mass per unit area is then modified locally, as is the complex bending stiffness. Outside the damping zone, the complex bending stiffness to be identified (i.e. derived from the actual material properties) is $(D/\mu)^{\text{w/o Damp.}} = 2.26$ m^4/s^2 whereas within this zone, it is $(D/\mu)^{\text{with Damp.}} = 2.14$ m^4/s^2. Here μ denoted the mass per unit area. The value of the real part of the bending stiffness normalised to mass per unit area in the damped zone is considered constant with frequency and as in the numerical study it is calculated using the modified value of the mass per unit area : $\mu = \mu^{\text{alu.}} + \mu^{\text{foam}}$, with $\mu^{\text{alu.}} = 2.6$ kg/m^2 and $\mu^{\text{foam}} = 0.15$ kg/m^2, while the bending stiffness of the foam material is considered negligible. The plate was attached to a frame by means of a clamping point and excited by a pseudo-random noise in the frequency range [100, 6400] Hz using a shaker. The position of the clamping point on the plate is (0.26, 0.52) m and the force is injected at the point (0.20, 0.23) m. The coordinates are given relative to the bottom left corner of the plate. The shaker is mounted on the plate using a nylon stinger. The displacement field was measured using a scanning laser vibrometer. The mesh consists again of 28×41 points with a spacing of $\Delta = 14.5$ mm. The dimensions of the measured area are 0.39×0.58 m^2. The set-up is shown in figure 12.

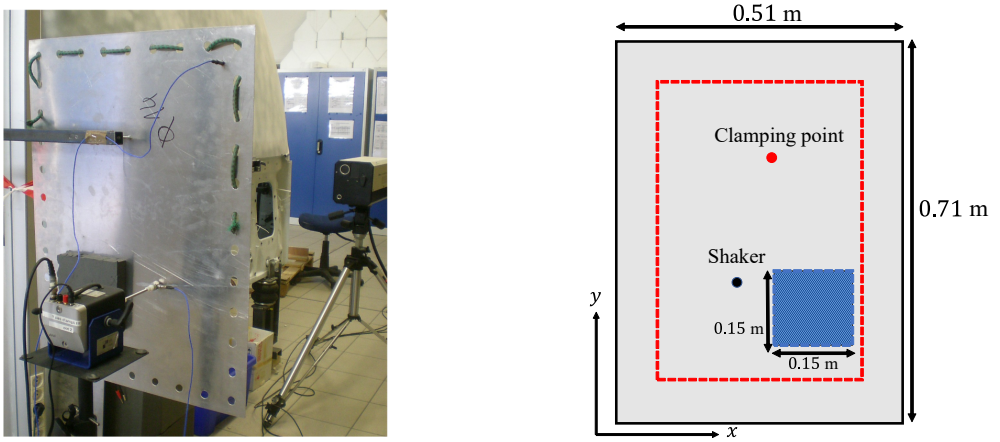

(a) (b)

Figure 12: Presentation of the experimental set-up, (a) Photo of the experimental set-up, (b) Scheme of the experimental set-up, the red rectangle bounds the measurement area and the blue area shows the added damping material. Figure from [16].

6.2. Identification of the complex bending stiffness with the Frequency-Adapted VFM and CFAT

The measured displacement field is first filtered. The filtering is performed in the wavenumber domain, using the following low-pass wavenumber filter response:

$$H(k_x, k_y) = \frac{1}{2}\left(1 - \tanh\left(\frac{\sqrt{k_x^2 + k_y^2} - \frac{k_c}{2\pi}}{0.3\frac{k_c}{2\pi}}\right)\right) \tag{37}$$

with $k_c = ak_{\text{f}}$ the cut-off wavenumber where a is a scalar greater than 1. The filtering operations are performed using the solution proposed in [41] which involves extrapolating the displacement field beyond the measured region. This extrapolation reduces the Gibbs phenomenon at the frontier of the measured region and avoids having to window the measured field. First, the displacement field is padded with zeros outside of the measured region. The wavenumber

transform of the zero-padded displacement field is calculated and low-passed filtered in the wavenumber domain using the filter described by eq. (37). An inverse wavenumber transform of the filtered field is computed to recover the displacement in the physical domain. Once this operation has been carried out, the measured field has been slightly extrapolated over the area where the zeros were added by the zero-padding operation. The area initially composed solely of the measured field has also been modified. Since these changes were not yet desired, the filtered displacement is replaced by the initial measured displacement into this zone. These operations are repeated until the difference between the displacement fields between two iterations is sufficiently small. At the end of the process, the low-passed displacement field is kept in the measurement region. This field has been passed through the low-pass filter of eq. (37) and, thanks to extrapolation, it is not affected by the Gibbs phenomenon without having been windowed.

Unlike the numerical study presented in section 5, the number of measurements points per wavelength at each frequency is unknown since wavelength depends on bending stiffness. Now, as indicated in section 4.4 it must be identified to apply the Frequency-Adapted VFM. This identification is achieved by applying the iterative process described in section 4.4. To do so, the complex bending stiffness is estimated at ω using the spatial least squares. The formalism of the spatial least squares is the same as the one introduced in section 5.3. The measurement points used to estimate $\mathbf{B}$ and $\mathbf{N}$ are located in a zone where no external load is applied and no damping is added. An average value of τ_{FA}^{0} is used as the initial value. Indeed, as pointed out in section 4.3, the values of τ_{FA}^{0}, $\tau_{\mathrm{FA}}^{\pi/3}$ or $\tau_{\mathrm{FA}}^{\pi/4}$ do not depend strongly on n. Referring to figure 7, this value is taken to be $\tau_{\mathrm{FA\,mean}}^{0} = 1.58$. Consequently, the iterative process is started using $\tau = 1.58$ and after the first estimate of n, the value τ_{FA}^{0} is determined using eq. (31). The process is carried out with 10 iterations. An advantage of this choice of initialization is that, since the first value of τ in the process is close to the true value of τ_{FA}^{0} for most values of n, the process converges easily and quickly.

Next, frequency least squares are applied. The formalism is the same as that described in section 5.2. The frequency least squares provide a map of the frequency averaged (in a least squares sense) identified bending stiffness (real part of the complex bending stiffness) and loss factor (ratio between the imaginary part and the real part of the identified complex bending stiffness). The results of this procedure using 1001 frequency points in the interval $[1000, 5000]$ Hz are shown in figure 13. The complex bending stiffness identified with CFAT and the Frequency-Adapted VFM are well recovered in the area where no external load is applied. Results of both methods are similar. The damping zone is clearly visible on the plots. Indeed, a decrease in the identified mass-normalised bending stiffness can be observed at the point where the damped material is glued. This decrease is caused by the added mass per unit area of the foam. In plots showing the loss factor, the damping zone is even more visible. In the region where the damped material is glued, a significant increase in the loss factor is observed on both maps (figures 13c and 13d). However, the loss factor identified with the Frequency-Adapted VFM is slightly higher than that identified with CFAT in the damping zone. At the clamping point and at the excitation point, singularities are present on all the maps. The reason, as already pointed in section 5.2, is that, in these zones, eqs. (14) and (32) are no longer valid, since a load is applied. The complex bending stiffness estimated by CFAT and the VFM is therefore erroneous. At the boundary between the damped and undamped zones, the finite-differences scheme, or virtual window, covers both zones. At this boundary, an average value for the loss factor or bending stiffness is obtained. However, as the domains remain large relative to the size of the virtual window or finite difference scheme, this problem is negligible. Overall, as both zones are clearly visible in figures 13b and 13d, the ability of FA VFM to identify a spatial distribution of stiffness and damping is well demonstrated and worthy of note.

Since the complex bending stiffness is correctly mapped, spatial least squares estimation can be applied to specific zones corresponding to zones with or without damping. So far, the complex bending stiffness has only been identified in space and the results presented in figure 13 correspond to an average value in a least squares sense of the complex bending stiffness over the frequency range $[1000, 5000]$ Hz. Therefore, to complete the caracterisation of the structure, identification at each frequency point is necessary. The Frequency-Adapted VFM and CFAT are then used to identify the bending stiffness and the loss factors of each zone. Calculations are performed in such a way that the finite difference scheme in CFAT, or the Newton interpolation zone in the VFM, is exclusively in a zone with or without damping. The complex bending stiffness estimated with CFAT at ω with the spatial least squares is obtained by the same process as the VFM (eq. (36)) but using eq. (14) instead of eq. (32). Now and below, the spatial least squares results at each frequency point and for each zone are obtained by considering all possible measurement points in each zone. To illustrate the beneficial use of the Frequency-Adapted virtual window length, Figure 14 shows the bending stiffness identified in a zone without damping or external forces for $\tau = 0$ and for $\tau = \tau_{\mathrm{FA}}^{0}$ as a function of frequency. The case where $\tau = 0$ is equivalent to a vanishingly small virtual window in eq. (32). The results below 1000 Hz are dominated by measurement

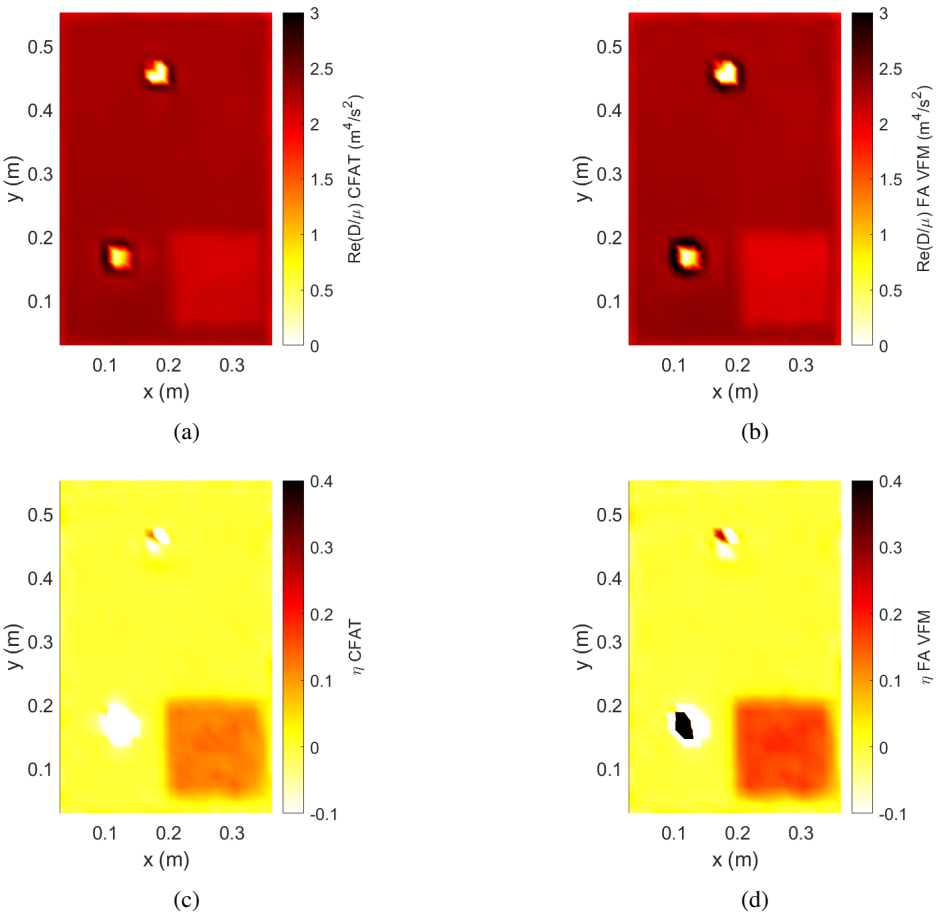

Figure 13: Bending stiffness and loss factor identified with CFAT and the Frequency-Adapted VFM using frequency least squares over the frequency range $[1000, 5000]$ Hz, (a) Real part of the complex bending stiffness identified with CFAT, (b) Real part of the complex bending stiffness identified with the Frequency-Adapted VFM, (c) Loss factor (ratio between the imaginary part and real part) identified with CFAT, (d) Loss factor identified with the Frequency-Adapted VFM.

noise. Indeed, if the size of the virtual window or finite difference scheme is small compared to the bending wavelength, the identified complex bending stiffness will be sensitive to measurement noise. As a consequence, the VFM for $\tau = 0$ and for $\tau = \tau_{\mathrm{FA}}^0$ will underestimate the complex bending stiffness. The effects of the Frequency-Adaptation process are clearly visible in figure 14. The bending stiffness identified with the VFM when $\tau = 0$ is overestimated at most frequencies, while that estimated when $\tau = \tau_{\mathrm{FA}}^0$ is close to the reference value at all frequencies above 1000 Hz. The overestimation observed when $\tau = 0$ is due to the singularity in the response of the method in the wavenumber domain. When $\tau = \tau_{\mathrm{FA}}^0$, the singularity is removed and, as a result, the complex bending stiffness is correctly identified at most frequencies.

Figure 15 shows the bending stiffness and loss factor obtained with the methods for both zones. Identification with the methods remains inaccurate below 1000 Hz. This error is again due to measurement noise. Above 1000 Hz, for both zones, the bending stiffness is well identified with both methods. Outside of the damped zone (figure 15a), the results of both methods match the reference values of 2.26 $\mathrm{m}^4/\mathrm{s}^2$ while inside the damped zone (figure 15b) the results of CFAT and FA VFM match the reference value of 2.14 $\mathrm{m}^4/\mathrm{s}^2$ calculated using the added mass per unit area of the damping material. The CFAT results are slightly different from those obtained with the Frequency-Adapted VFM, particularly at high frequencies. Regarding the loss factor, outside the damping zone, the values to be identified are too low for the methods to identify it correctly. However, in the damping zone, both methods show a significant increase in the identified loss factor. The Frequency-Adapted VFM estimate of the loss factor is higher than the CFAT estimate.

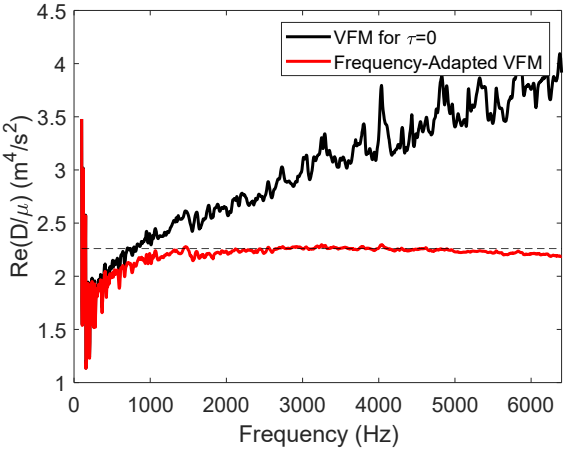

Figure 14: Identified bending stiffness with the VFM for $\tau = 0$ (black line) and for $\tau = \tau_{\text{FA}}^{0}$ using eq. (31) (red line). The horizontal black dotted line corresponds to $(D/\mu)^{\text{w/o Damp.}}$

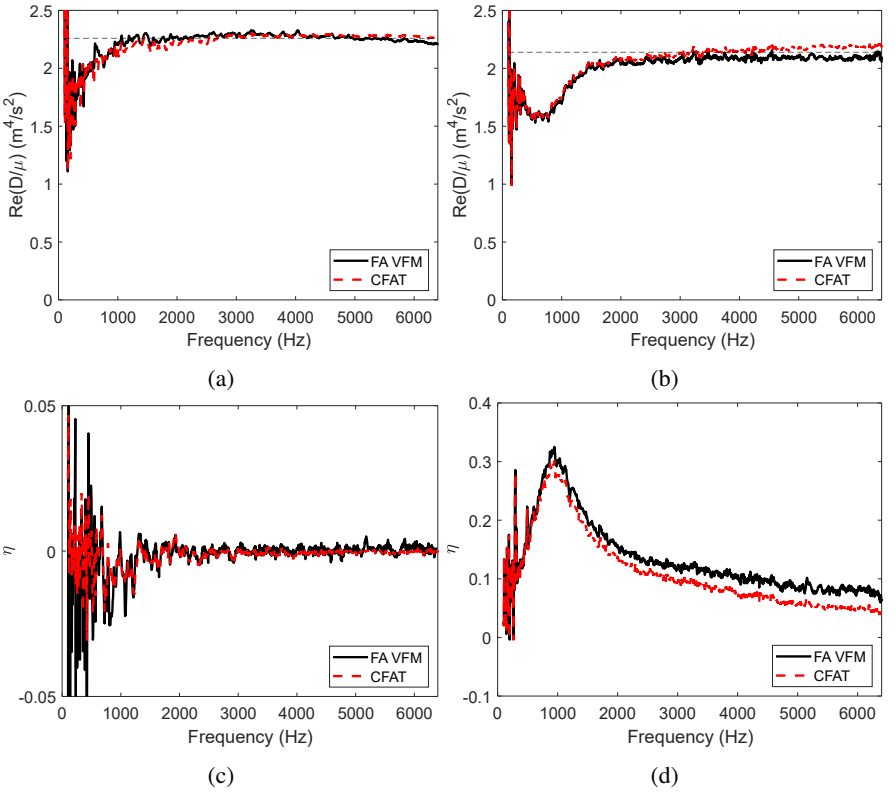

Figure 15: Bending stiffness and loss factor identified with the Frequency-Adapted VFM and CFAT using spatial least squares, (a) Bending stiffness identified on the zone without damping (the horizontal black dotted line corresponds to $(D/\mu)^{\text{w/o Damp.}}$), (b) Bending stiffness identified on the zone with damping (the horizontal black dotted line corresponds to $(D/\mu)^{\text{with Damp.}}$), (c) η identified on the zone without damping, (d) η identified on the zone with damping.

This observation is similar to that made with regard to the results presented in section 5.3 in the numerical study. The poorer suppression of the singularity in the FA VFM response may be the reason for these slight differences. Overall, the consistency between the CFAT and the FA VFM results validates the proposed FA VFM.

6.3. Use of an average value of τ_{FA}

The iterative process used at the beginning of section 6.2 is a drawback of both CFAT and the FA VFM. Although this process cannot be avoided when CFAT is applied, the use of the average value of τ_{FA} mentioned in section 6.2 may be a solution to eliminate this iterative process when the FA VFM is applied. So, instead of calculating the corresponding value of τ_{FA} at each frequency, it is possible to use $\tau^0_{\mathrm{FA\ mean}} = 1.58$ over the whole frequency range considered in the study. It is, then, no longer necessary to determine the number of points per wavelength, since the exact value of τ_{FA} is not determined at every frequency. As a result, the iterative process is no longer necessary. Note that, in [35], this mean value has already been used to determine the bending stiffness of an Euler-Bernoulli beam.
The results presented in section 6.2 are reintroduced, but now also using $\tau^0_{\mathrm{FA\ mean}}$. First, frequency least squares are applied using eq. (34) and the mean value of $\tau^0_{\mathrm{FA\ mean}}$. Figure 16 shows the resulting maps of the bending stiffness and loss factor. The bending stiffness (figure 16a) is well identified in both zones. Once again, singularities are observed

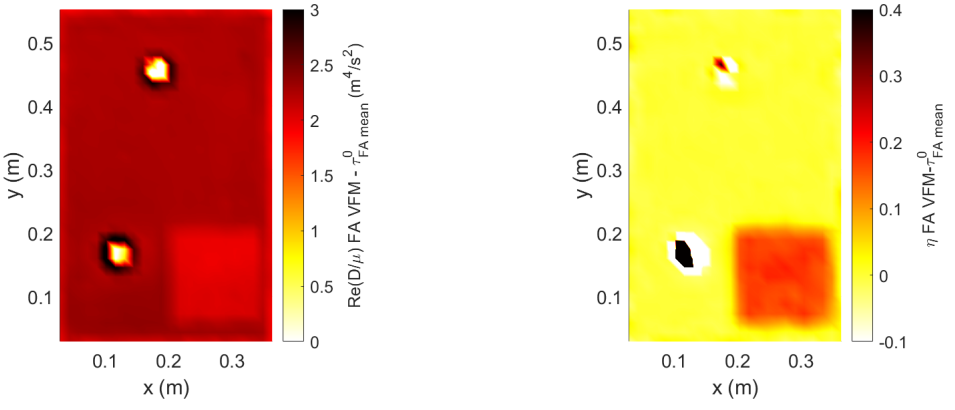

(a) (b)

Figure 16: Bending stiffness and loss factor identified with the VFM for $\tau = \tau^0_{\mathrm{FA\ mean}}$ using frequency least squares over the frequency range $[1000, 5000]$ Hz, (a) Real part of the complex bending stiffness, (d) Loss factor.

at the clamping point and at the excitation point. In addition, the damping zone is correctly identified as a zone of decreased bending stiffness. With regard to the loss factor (figure 16b), the results are also consistent. The damped zone shows a large increase of the loss factor. The results are similar to those obtained with FA VFM (figure 13). Indeed, between $[1000, 5000]$, the number of points per wavelength is between 6.62 and 2.97. So, referring to figure 7, for most of the frequency points considered in this interval, the exact value of τ^0_{FA} is close to the mean value.
Once again, the results presented in figure 16 only show a spatial mapping of the frequency-averaged identified complex bending stiffness. Therefore, an additional identification based on spatial least squares is now applied using eq. (36). Figure 17 shows the bending stiffness and loss factor identified with VFM for $\tau = \tau^0_{\mathrm{FA\ mean}}$ on each zone. The results are compared with those of FA VFM. In the undamped and damped zones, the bending stiffness is well identified at most frequencies (figures 17a and 17b). Again, below 1000 Hz, the results are dominated by measurement noise, leading to an underestimation of the identified bending stiffness. With regard to the loss factor, outside the damped zone (figure 17c), the values are once again too low to be properly identified. In the damped zone (figure 17d), the increase in the loss factor due to the added damped material is clearly observed. Globally, the results obtained with VFM for $\tau = \tau^0_{\mathrm{FA\ mean}}$ are then generally in line with those obtained with CFAT and the FA VFM. The main differences are in the bending stiffness plots (figures 17a and 17b). Although the results remain in line with those of FA VFM, it should be pointed out that as frequency increases, the VFM estimate of bending stiffness in both zones for $\tau = \tau^0_{\mathrm{FA\ mean}}$ becomes less accurate. Indeed, when n becomes small, $\tau^0_{\mathrm{FA\ mean}}$ starts to deviate from the true value of τ^0_{FA} (figure 7) and, therefore, a larger estimation error can be expected. This was observed in [35]. However, although the results deteriorate in higher frequencies, they remain consistent. This result can be explained by the fact that if $\tau^0_{\mathrm{FA\ mean}}$ is far from the exact value of τ^0_{FA} when n is small, it is not for other angular directions in the calculation of τ_{FA}. So, when $\tau^0_{\mathrm{FA\ mean}}$ is used, the singularity at the circle $\sqrt{k_x^2 + k_y^2} = k_{\mathrm{f}}$ remains suppressed even when n is small. It is not suppressed at the point of the circle with angular direction $\theta = 0$ but at another point. Therefore, even if n is small,

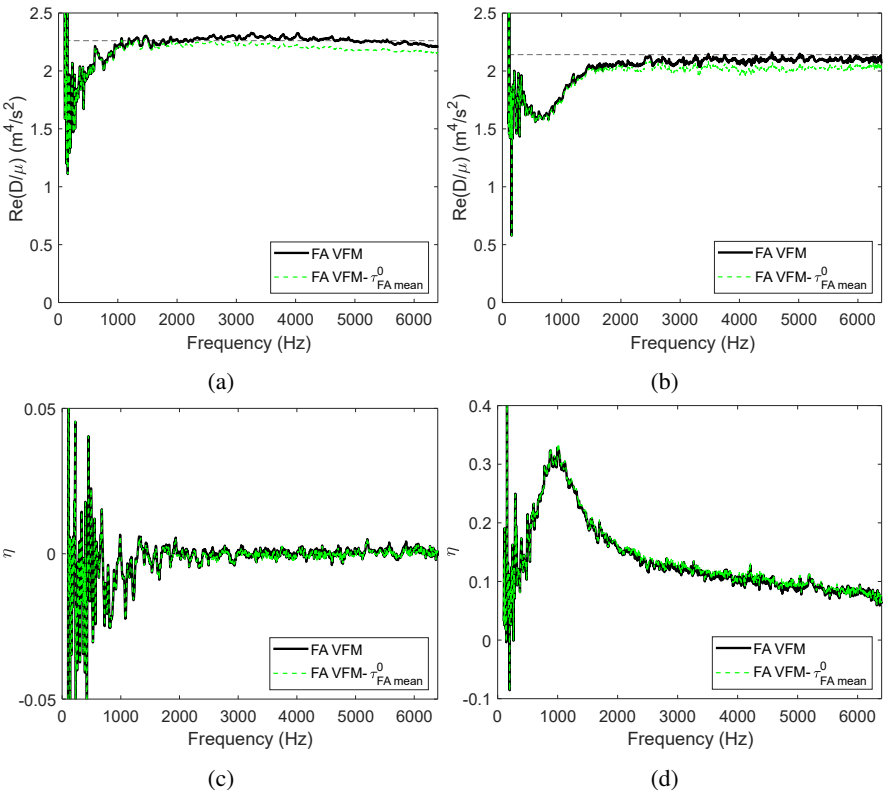

Figure 17: Bending stiffness and loss factor identified with the Frequency-Adapted VFM and the VFM for $\tau = \tau^0_{\text{FA mean}}$ using spatial least squares, (a) Bending stiffness identified on the zone without damping (the horizontal black dotted line corresponds to $(D/\mu)^{\text{w/o Damp.}}$) (b) Bending stiffness identified on the zone with damping (the horizontal black dotted line corresponds to $(D/\mu)^{\text{with Damp.}}$), (c) η identified on the zone without damping, (d) η identified on the zone with damping

using $\tau^0_{\text{FA mean}}$ instead of the exact value of τ^0_{FA} still yields consistent values. However, as pointed out in section 4.3, the value τ^0_{FA} remains the value of τ_{FA} that best suppresses the singularity at the circle $\sqrt{k_x^2 + k_y^2} = k_{\text{f}}$. It is therefore logical that the results deteriorate as the value used for τ is further away from the actual value of τ^0_{FA}.
Note that the error in this case remains reasonably small because the minimum value of n in this study is 2.6. If the minimum value of n had been lower, the error obtained using $\tau^0_{\text{FA mean}}$ should have been greater.

6.4. Comparison between the Frequency-Adapted VFM and the Conventional-VFM

The Frequency-Adapted VFM is now compared with the classical VFM approach, referred to as the Conventional-VFM (C-VFM) for the sake of clarity. In the Conventional-VFM, the PVW integrals in eq. (16) are calculated numerically using trapezoidal integration whereas in the Frequency-Adapted VFM they are calculated analytically. Since a large number of measurement points is required to estimate the PWV integrals correctly, the measured displacement field is oversampled by multiplying the number of measurement points by 3 using the Matlab® *interp2* function. As a result of this interpolation operation, the spacing between measurement points is divided by 3, from $\Delta = 14.5$ mm to $\Delta_i = 4.8$ mm. Curvatures are obtained by numerical differentiation of oversampled displacements. Note that this operation follows the same idea as that used with FA VFM when the displacement field is interpolated. Indeed, as indicated in the section 4.2, interpolation consists of increasing the number of points used in the calculation of integrals, which makes it possible to obtain a better estimate. The Conventional-VFM is then applied to identify the complex bending stiffness of the plate using a 9×9 virtual window placed over the oversampled fields. The size of the virtual window has been determined to be consistent with the sizes proposed in [31]. Note that the virtual fields are the same as those used for the Frequency-Adapted VFM. The Conventional-VFM is first applied to identify the bending stiffness at each frequency using the spatial least-squares approach (eq. (36)) in the zone with damping and in

the zone without damping. The results are shown in figure 18. These results are compared with those of the Frequency-Adapted VFM. Figures 18a and 18b show that the bending stiffness of the plate identified with the Conventional-VFM

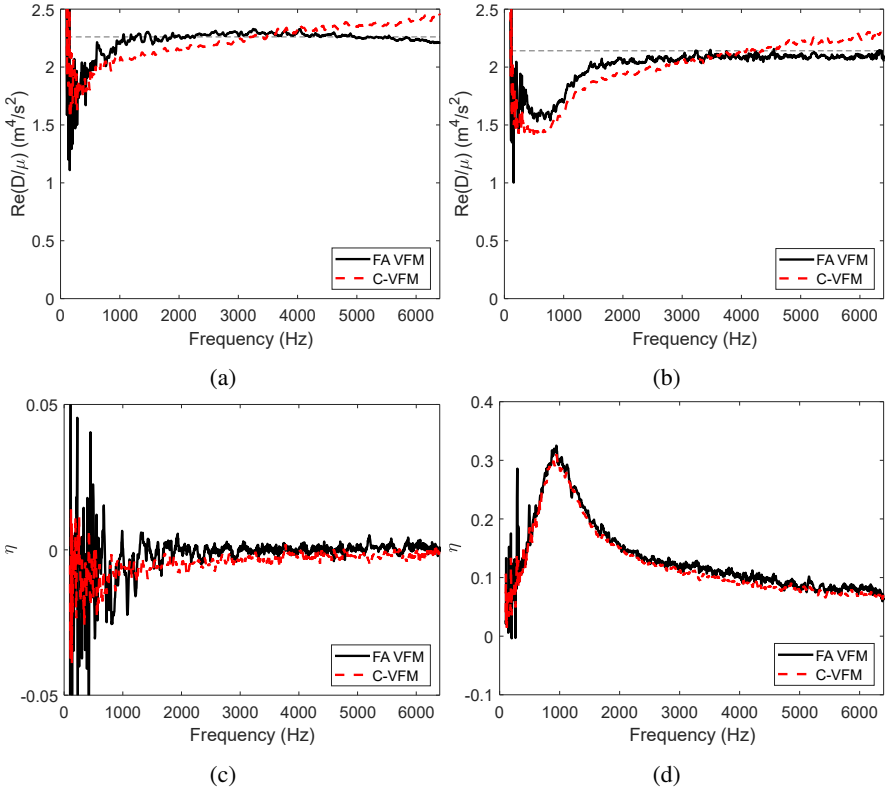

Figure 18: Bending stiffness and loss factor identified with the Frequency-Adapted VFM and the Conventional-VFM using spatial least squares, (a) Bending stiffness identified on the area without damping (the horizontal black dotted line corresponds to $(D/\mu)^{\text{w/o Damp.}}$), (b) Bending stiffness identified on the area with damping (the horizontal black dotted line corresponds to $(D/\mu)^{\text{with Damp.}}$), (c) η identified on the area without damping, (d) η identified on the area with damping

is underestimated below 3 kHz and overestimated above 3 kHz as compared to the Frequency-Adapted VFM. The results in the damping zone (figure 18b) are those where the identified bending stiffness is furthest from the reference value. These results may be explained by the lack of measurement points on the virtual window and therefore in the PVW interval estimation (eq. (16)). This lack of points is due to the small size of the damping zone. Note that the loss factor η identified with the Conventional-VFM is consistent with that identified with the Frequency-Adapted VFM inside the damping zone (figure 18d). Outside the damping zone, the loss factor to be identified is too low for the Conventional-VFM to identify it correctly. Finally, the Conventional-VFM is applied to identify the complex bending stiffness at each point of the structure using all frequencies in the interval $f \in [1000, 5000]$ Hz and the frequency least squares approach (eq. (34)). As in sections 6.2 and 6.3, these results complete the characterisation of the structure carried out by the method. They are shown in figure 19. The results obtained with the Conventional-VFM compare well with those obtained with the Frequency-Adapted VFM. The bending stiffness is clearly identified for each zone, as is the loss factor. Indeed, the decrease in bending stiffness and the increase in the loss factor can be clearly seen on both maps at the location of the damping material. Note that the singularities at the clamping point and the force injection point are also clearly visible on the maps. Overall, the Conventional-VFM performs well. However, the method requires a large number of points to estimate the integrals in the PVW. These good results are mainly due to the oversampling of the displacement field, which multiplies the number of points per wavelength by 3 in this case. On the other hand, thanks to polynomial interpolation, the Frequency-Adapted VFM does not need a large number of measurement points to give good results, so no oversampling is required. This is an advantage of the proposed approach.

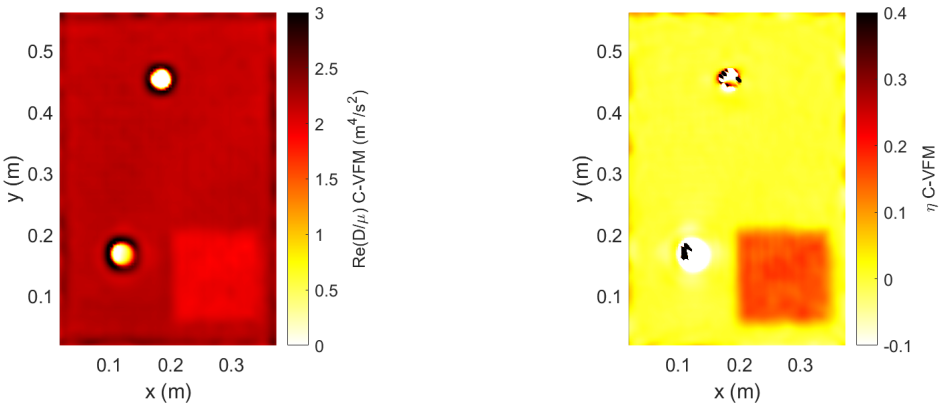

(a) (b)

Figure 19: Bending stiffness and loss factor identified with the Conventional-VFM using frequency least squares over the frequency range $[1000, 5000]$ Hz, (a) Real part of the complex bending stiffness, (b) Loss factor.

7. Conclusion

This paper has presented the extension of the Frequency-Adapted VFM presented in [35] to the 2D case to identify the bending stiffness and loss factor of a Love-Kirchhoff plate. The VFM consists in choosing a test function called virtual displacement to solve the Principle of Virtual Work. In this work, virtual fields are piecewise functions defined over a virtual window. The Frequency-Adaptation process involves polynomial interpolation of the measured displacement field and finding the virtual window size that removes the singularity of the method at the free bending wavenumber. Indeed, the response of the method in the wavenumber domain presents a singularity on a circle of radius equal to the bending wavenumber of the plate. The Frequency-Adapted size for the virtual window is the one that eliminates the singularity at a given point on the circle. Experimental results based on Laser Doppler Velocimetry (LDV) data on an aluminum plate partially covered with a damping material from [16] have been presented. Spatial and frequency least squares have been applied to identify the complex bending stiffness in both space and frequency. These experimental results have shown that the FA VFM can be used to identify complex bending stiffness over a wide range of frequencies. Using frequency least squares, the ability of Frequency-Adapted VFM to identify spatial variations in bending stiffness and damping was well demonstrated. This was illustrated by the presentation of bending stiffness and damping maps, where damped and undamped areas are clearly visible. The Frequency-Adapted VFM results were compared with CFAT and the Conventional-VFM results. The results of the FA VFM are almost always similar with of those of CFAT. In the Conventional-VFM, PVW integrals are calculated using trapezoidal integration and the displacement field must therefore be oversampled before applying the method. In future work, the Frequency-Adapted VFM will be extended to more complex panels to identify bending stiffness and loss factor.

Acknowledgement

This study was funded by the Fonds de recherche du Québec - Nature et technologies (FRQNT) and was performed within the framework of the Labex CeLyA of Université de Lyon, operated by the French National Research Agency (ANR-10-LABX- 0060/ ANR-11-IDEX0007).

Appendix A : Interpolation of the measured displacement field

The matrix **P** in eq. (21) is defined by :

$$\mathbf{P} = \begin{pmatrix} P_{1,1} & P_{2,1} & P_{3,1} & P_{4,1} & P_{5,1} \\ P_{1,2} & P_{2,2} & P_{3,2} & P_{4,2} & P_{5,2} \\ P_{1,3} & P_{2,3} & P_{3,3} & P_{4,3} & P_{5,3} \\ P_{1,4} & P_{2,4} & P_{3,4} & P_{4,4} & P_{5,4} \\ P_{1,5} & P_{2,5} & P_{3,5} & P_{4,5} & P_{5,5} \end{pmatrix}$$

with,

$$P_{1,1} = \tilde{w}_{1,1}, \quad P_{2,1} = \tilde{w}_{1,2} - \tilde{w}_{1,1}, \quad P_{3,1} = \frac{\tilde{w}_{1,1}}{2} - \tilde{w}_{1,2} + \frac{\tilde{w}_{1,3}}{2}, \quad P_{4,1} = \frac{\tilde{w}_{1,2}}{2} - \frac{\tilde{w}_{1,1}}{6} - \frac{\tilde{w}_{1,3}}{2} + \frac{\tilde{w}_{1,4}}{6}$$

$$P_{5,1} = \frac{\tilde{w}_{1,1}}{24} - \frac{\tilde{w}_{1,2}}{6} + \frac{\tilde{w}_{1,3}}{4} - \frac{\tilde{w}_{1,4}}{6} + \frac{\tilde{w}_{1,5}}{24}, \quad P_{1,2} = \tilde{w}_{2,1} - \tilde{w}_{1,1}, \quad P_{2,2} = \tilde{w}_{1,1} - \tilde{w}_{1,2} - \tilde{w}_{2,1} + \tilde{w}_{2,2},$$

$$P_{3,2} = \tilde{w}_{1,2} - \frac{\tilde{w}_{1,1}}{2} - \frac{\tilde{w}_{1,3}}{2} + \frac{\tilde{w}_{2,1}}{2} - \tilde{w}_{2,2} + \frac{\tilde{w}_{2,3}}{2}, \quad P_{4,2} = \frac{\tilde{w}_{1,1}}{6} - \frac{\tilde{w}_{1,2}}{2} + \frac{\tilde{w}_{1,3}}{2} - \frac{\tilde{w}_{1,4}}{6} - \frac{\tilde{w}_{2,1}}{6} + \frac{\tilde{w}_{2,2}}{2} - \frac{\tilde{w}_{2,3}}{2} + \frac{\tilde{w}_{2,4}}{6},$$

$$P_{5,2} = \frac{\tilde{w}_{1,2}}{6} - \frac{\tilde{w}_{1,1}}{24} - \frac{\tilde{w}_{1,3}}{4} + \frac{\tilde{w}_{1,4}}{6} - \frac{\tilde{w}_{1,5}}{24} + \frac{\tilde{w}_{2,1}}{24} - \frac{\tilde{w}_{2,2}}{6} + \frac{\tilde{w}_{2,3}}{4} - \frac{\tilde{w}_{2,4}}{6} + \frac{\tilde{w}_{2,5}}{24}, \quad P_{1,3} = \frac{\tilde{w}_{1,1}}{2} - \tilde{w}_{2,1} + \frac{\tilde{w}_{3,1}}{2},$$

$$P_{2,3} = \frac{\tilde{w}_{1,2}}{2} - \frac{\tilde{w}_{1,1}}{2} + \tilde{w}_{2,1} - \tilde{w}_{2,2} - \frac{\tilde{w}_{3,1}}{2} + \frac{\tilde{w}_{3,2}}{2}, \quad P_{3,3} = \frac{\tilde{w}_{1,1}}{4} - \frac{\tilde{w}_{1,2}}{2} + \frac{\tilde{w}_{1,3}}{4} - \frac{\tilde{w}_{2,1}}{2} + \tilde{w}_{2,2} - \frac{\tilde{w}_{2,3}}{2} + \frac{\tilde{w}_{3,1}}{4} - \frac{\tilde{w}_{3,2}}{2} + \frac{\tilde{w}_{3,3}}{4},$$

$$P_{4,3} = \frac{\tilde{w}_{1,2}}{4} - \frac{\tilde{w}_{1,1}}{12} - \frac{\tilde{w}_{1,3}}{4} + \frac{\tilde{w}_{1,4}}{12} + \frac{\tilde{w}_{2,1}}{6} - \frac{\tilde{w}_{2,2}}{2} + \frac{\tilde{w}_{2,3}}{2} - \frac{\tilde{w}_{2,4}}{6} - \frac{\tilde{w}_{3,1}}{12} + \frac{\tilde{w}_{3,2}}{4} - \frac{\tilde{w}_{3,3}}{4} + \frac{\tilde{w}_{3,4}}{12},$$

$$P_{5,3} = \frac{\tilde{w}_{1,1}}{48} - \frac{\tilde{w}_{1,2}}{12} + \frac{\tilde{w}_{1,3}}{8} - \frac{\tilde{w}_{1,4}}{12} + \frac{\tilde{w}_{1,5}}{48} - \frac{\tilde{w}_{2,1}}{24} + \frac{\tilde{w}_{2,2}}{6} - \frac{\tilde{w}_{2,3}}{4} + \frac{\tilde{w}_{2,4}}{6} - \frac{\tilde{w}_{2,5}}{24} + \frac{\tilde{w}_{3,1}}{48} - \frac{\tilde{w}_{3,2}}{12} + \frac{\tilde{w}_{3,3}}{8} - \frac{\tilde{w}_{3,4}}{12} + \frac{\tilde{w}_{3,5}}{48},$$

$$P_{1,4} = \frac{\tilde{w}_{2,1}}{2} - \frac{\tilde{w}_{1,1}}{6} - \frac{\tilde{w}_{3,1}}{2} + \frac{\tilde{w}_{4,1}}{6}, \quad P_{2,4} = \frac{\tilde{w}_{1,1}}{6} - \frac{\tilde{w}_{1,2}}{6} - \frac{\tilde{w}_{2,1}}{2} + \frac{\tilde{w}_{2,2}}{2} + \frac{\tilde{w}_{3,1}}{2} - \frac{\tilde{w}_{3,2}}{2} - \frac{\tilde{w}_{4,1}}{6} + \frac{\tilde{w}_{4,2}}{6},$$

$$P_{3,4} = \frac{\tilde{w}_{1,2}}{6} - \frac{\tilde{w}_{1,1}}{12} - \frac{\tilde{w}_{1,3}}{12} + \frac{\tilde{w}_{2,1}}{4} - \frac{\tilde{w}_{2,2}}{2} + \frac{\tilde{w}_{2,3}}{4} - \frac{\tilde{w}_{3,1}}{4} + \frac{\tilde{w}_{3,2}}{2} - \frac{\tilde{w}_{3,3}}{4} + \frac{\tilde{w}_{4,1}}{12} - \frac{\tilde{w}_{4,2}}{6} + \frac{\tilde{w}_{4,3}}{12},$$

$$P_{4,4} = \frac{\tilde{w}_{1,1}}{36} - \frac{\tilde{w}_{1,2}}{12} + \frac{\tilde{w}_{1,3}}{12} - \frac{\tilde{w}_{1,4}}{36} - \frac{\tilde{w}_{2,1}}{12} + \frac{\tilde{w}_{2,2}}{4} - \frac{\tilde{w}_{2,3}}{4} + \frac{\tilde{w}_{2,4}}{12} + \frac{\tilde{w}_{3,1}}{12} - \frac{\tilde{w}_{3,2}}{4} + \frac{\tilde{w}_{3,3}}{4} - \frac{\tilde{w}_{3,4}}{12} - \frac{\tilde{w}_{4,1}}{36} + \ldots$$
$$\frac{\tilde{w}_{4,2}}{12} - \frac{\tilde{w}_{4,3}}{12} + \frac{\tilde{w}_{4,4}}{36},$$

$$P_{5,4} = \frac{\tilde{w}_{1,2}}{36} - \frac{\tilde{w}_{1,1}}{144} - \frac{\tilde{w}_{1,3}}{24} + \frac{\tilde{w}_{1,4}}{36} - \frac{\tilde{w}_{1,5}}{144} + \frac{\tilde{w}_{2,1}}{48} - \frac{\tilde{w}_{2,2}}{12} + \frac{\tilde{w}_{2,3}}{8} - \frac{\tilde{w}_{2,4}}{12} + \frac{\tilde{w}_{2,5}}{48} - \frac{\tilde{w}_{3,1}}{48} + \frac{\tilde{w}_{3,2}}{12} - \frac{\tilde{w}_{3,3}}{8} + \frac{\tilde{w}_{3,4}}{12} - \ldots$$
$$\frac{\tilde{w}_{3,5}}{48} + \frac{\tilde{w}_{4,1}}{144} - \frac{\tilde{w}_{4,2}}{36} + \frac{\tilde{w}_{4,3}}{24} - \frac{\tilde{w}_{4,4}}{36} + \frac{\tilde{w}_{4,5}}{144},$$

$$P_{1,5} = \frac{\tilde{w}_{1,1}}{24} - \frac{\tilde{w}_{2,1}}{6} + \frac{\tilde{w}_{3,1}}{4} - \frac{\tilde{w}_{4,1}}{6} + \frac{\tilde{w}_{5,1}}{24},$$

$$P_{2,5} = \frac{\tilde{w}_{1,2}}{24} - \frac{\tilde{w}_{1,1}}{24} + \frac{\tilde{w}_{2,1}}{6} - \frac{\tilde{w}_{2,2}}{6} - \frac{\tilde{w}_{3,1}}{4} + \frac{\tilde{w}_{3,2}}{4} + \frac{\tilde{w}_{4,1}}{6} - \frac{\tilde{w}_{4,2}}{6} - \frac{\tilde{w}_{5,1}}{24} + \frac{\tilde{w}_{5,2}}{24},$$

$$P_{3,5} = \frac{\tilde{w}_{1,1}}{48} - \frac{\tilde{w}_{1,2}}{24} + \frac{\tilde{w}_{1,3}}{48} - \frac{\tilde{w}_{2,1}}{12} + \frac{\tilde{w}_{2,2}}{6} - \frac{\tilde{w}_{2,3}}{12} + \frac{\tilde{w}_{3,1}}{8} - \frac{\tilde{w}_{3,2}}{4} + \frac{\tilde{w}_{3,3}}{8} - \frac{\tilde{w}_{4,1}}{12} + \frac{\tilde{w}_{4,2}}{6} - \frac{\tilde{w}_{4,3}}{12} + \frac{\tilde{w}_{5,1}}{48} - \frac{\tilde{w}_{5,2}}{24} + \frac{\tilde{w}_{5,3}}{48},$$

$$P_{4,5} = \frac{\tilde{w}_{1,2}}{48} - \frac{\tilde{w}_{1,1}}{144} - \frac{\tilde{w}_{1,3}}{48} + \frac{\tilde{w}_{1,4}}{144} + \frac{\tilde{w}_{2,1}}{36} - \frac{\tilde{w}_{2,2}}{12} + \frac{\tilde{w}_{2,3}}{12} - \frac{\tilde{w}_{2,4}}{36} - \frac{\tilde{w}_{3,1}}{24} + \frac{\tilde{w}_{3,2}}{8} - \frac{\tilde{w}_{3,3}}{8} + \frac{\tilde{w}_{3,4}}{24} + \frac{\tilde{w}_{4,1}}{36} - \frac{\tilde{w}_{4,2}}{12} + \ldots$$
$$\frac{\tilde{w}_{4,3}}{12} - \frac{\tilde{w}_{4,4}}{36} - \frac{\tilde{w}_{5,1}}{144} + \frac{\tilde{w}_{5,2}}{48} - \frac{\tilde{w}_{5,3}}{48} + \frac{\tilde{w}_{5,4}}{144},$$

$$P_{5,5} = \frac{\tilde{w}_{1,1}}{576} - \frac{\tilde{w}_{1,2}}{144} + \frac{\tilde{w}_{1,3}}{96} - \frac{\tilde{w}_{1,4}}{144} + \frac{\tilde{w}_{1,5}}{576} - \frac{\tilde{w}_{2,1}}{144} + \frac{\tilde{w}_{2,2}}{36} - \frac{\tilde{w}_{2,3}}{24} + \frac{\tilde{w}_{2,4}}{36} - \frac{\tilde{w}_{2,5}}{144} + \frac{\tilde{w}_{3,1}}{96} - \frac{\tilde{w}_{3,2}}{24} + \frac{\tilde{w}_{3,3}}{16} - \frac{\tilde{w}_{3,4}}{24} + \dots$$
$$\frac{\tilde{w}_{3,5}}{96} - \frac{\tilde{w}_{4,1}}{144} + \frac{\tilde{w}_{4,2}}{36} - \frac{\tilde{w}_{4,3}}{24} + \frac{\tilde{w}_{4,4}}{36} - \frac{\tilde{w}_{4,5}}{144} + \frac{\tilde{w}_{5,1}}{576} - \frac{\tilde{w}_{5,2}}{144} + \frac{\tilde{w}_{5,3}}{96} - \frac{\tilde{w}_{5,4}}{144} + \frac{\tilde{w}_{5,5}}{576}.$$

Appendix B : Coefficients A_i and B_i

The coefficients A_i and B_i in eq. (26) are given by,

$$\begin{aligned}
A_0 &= 1 - \frac{5\tau^2}{14} + \frac{131\tau^4}{2352} - \frac{5\tau^6}{1176} + \frac{\tau^8}{7056}, \quad B_0 = \frac{49}{2} - \frac{45\tau^2}{7} + \frac{25\tau^4}{49}, \\
A_1 &= \frac{4\tau^4}{441} - \frac{2\tau^6}{1323} + \frac{\tau^8}{15876}, \quad B_1 = \frac{32}{9} - \frac{16\tau^2}{7} + \frac{100\tau^4}{441}, \\
A_2 &= \frac{\tau^4}{28224} - \frac{\tau^6}{42336} + \frac{\tau^8}{254016}, \quad B_2 = \frac{1}{72} - \frac{\tau^2}{28} + \frac{25\tau^4}{1764}, \\
A_3 &= -\frac{\tau^4}{1764} + \frac{5\tau^6}{21168} - \frac{\tau^8}{63504}, \quad B_3 = -\frac{2}{9} + \frac{5\tau^2}{14} + \frac{25\tau^4}{441}, \\
A_4 &= -\frac{\tau^2}{168} + \frac{43\tau^4}{14112} - \frac{\tau^6}{2352} + \frac{\tau^8}{42336}, \quad B_4 = \frac{17}{12} - \frac{9\tau^2}{14} + \frac{25\tau^4}{294}, \\
A_5 &= \frac{2\tau^2}{21} - \frac{11\tau^4}{441} + \frac{\tau^6}{392} - \frac{\tau^8}{10584} \text{ and } B_5 = -\frac{32}{3} + \frac{27\tau^2}{7} - \frac{50\tau^4}{147}.
\end{aligned} \tag{B.1}$$

References

[1] F. Ablitzer, C. Pézerat, J.-M. Génevaux, J. Bégué, Identification of stiffness and damping properties of plates by using the local equation of motion, J. Sound Vib. 333 (2014) 2454–2468, DOI: 10.1016/j.jsv.2013.12.013.

[2] K. Ege, X. Boutillon, B. David, High-resolution modal analysis, J. Sound Vib. 325 (2009) 852–869, DOI: 10.1016/j.jsv.2009.04.019.

[3] F. Marchetti, Modélisation et caractérisation large bande de plaques multicouches anisotropes (Modelling and characterisation of anisotropic multilayered plates on a wide frequency range), PhD thesis, Lyon, France: Institut National des Sciences Appliquées de Lyon, 2019, 179 pages, URL: https://www.researchgate.net/publication/338736309_Modelisation_et_caracterisation_large_bande_de_plaques_multicouches_anisotropes.

[4] P. Margerit, A. Lebée, J.-F. Caron, K. Ege, X. Boutillon, The High-Resolution Wavevector Analysis for the characterization of the dynamic response of composite plates, J. Sound Vib. 458 (2019) 177–196, DOI: 10.1016/j.jsv.2019.06.026.

[5] X. Li, M. Ichchou, A. Zine, C. Droz, N. Bouhaddi, An Algebraic Wavenumber Identification (AWI) technique under stochastic conditions, Mech. Syst. Sig. Process. 188 (2023) 109983, DOI: 10.1016/j.ymssp.2022.109983.

[6] J. Berthaut, M. N. Ichchou, L. Jezequel, K-space identification of apparent structural behaviour, J. Sound Vib. 280 (2005) 1125–1131, DOI: 10.1016/j.jsv.2004.02.044.

[7] F. Marchetti, N. Roozen, J. Segers, K. Ege, M. Kersemans, Q. Leclère, Experimental methodology to assess the dynamic equivalent stiffness properties of elliptical orthotropic plates, J. Sound Vib. 495 (2021) 115897, DOI: 10.1016/j.jsv.2020.115897.

[8] N. B. Roozen, Q. Leclère, K. Ege, Y. Gerges, Estimation of plate material properties by means of a complex wavenumber fit using Hankel's functions and the image source method, J. Sound Vib. 390 (2017) 257–271, DOI: 10.1016/j.jsv.2016.11.037.

[9] Y. Mei, S. Goenezen, Mapping the Viscoelastic Behavior of Soft Solids From Time Harmonic Motion, J. Appl. Mech. 85 (4) (2018) 041003, DOI: 10.1115/1.4038966.

[10] L. Tan, M. D. J. McGarry, E. E. W. Van Houten, M. Ji, L. Solamen, J. B. Weaver, K. D. Paulsen, Gradient-Based Optimization for Poroelastic and Viscoelastic MR Elastography, IEEE Trans. Med. Imaging 36 (1) (2017) 236–250, DOI: 10.1109/TMI.2016.2604568.

[11] C. Pézerat, J.-L. Guyader, Two inverse methods for localization of external sources exciting a beam, Acta Acustica 3 (1995) 1–10, URL: https://www.researchgate.net/publication/275657452_Two_inverse_methods_for_localization_of_external_sources_exciting_a_beam.

[12] C. Pézerat, J.-L. Guyader, Identification of vibration sources, Appl. Acoust. 61 (2000) 309–324, DOI: 10.1016/S0003-682X(00)00036-0.

[13] F. Ablitzer, C. Pézerat, B. Lascoup, J. Brocail, Identification of the flexural stiffness parameters of an orthotropic plate from the local dynamic equilibrium without a priori knowledge of the principal directions, J. Sound Vib. 404 (2017) 31–46, DOI: 10.1016/j.jsv.2017.05.037.

[14] T. Wassereau, F. Ablitzer, C. Pézerat, J.-L. Guyader, Experimental identification of flexural and shear complex moduli by inverting the Timoshenko beam problem, J. Sound Vib. 399 (2017) 86–103, DOI: 10.1016/j.jsv.2017.03.017.

[15] Q. Leclère, C. Pézerat, Vibration source identification using corrected finite difference schemes, J. Sound Vib. 331 (2012) 1366–1377, DOI: 10.1016/j.jsv.2011.11.002.

[16] Q. Leclère, F. Ablitzer, C. Pézerat, Practical implementation of the corrected force analysis technique to identify the structural parameter and load distributions, J. Sound Vib. 351 (2015) 106–118, DOI: 10.1016/j.jsv.2015.04.025.

[17] F. Marchetti, K. Ege, Q. Leclère, Development of the Corrected Force Analysis Technique for laminated composite panels, J. Sound Vib. 490 (2021) 115692, DOI: 10.1016/j.jsv.2020.115692.

[18] K. Ege, N. Roozen, Q. Leclère, R. G. Rinaldi, Assessment of the apparent bending stiffness and damping of multilayer plates; modelling and experiment, J. Sound Vib. 426 (2018) 129–149, DOI: 10.1016/j.jsv.2018.04.013.

[19] A. Giraudeau, F. Pierron, Identification of stiffness and damping properties of thin isotropic vibrating plates using the virtual fields method: theory and simulations, J. Sound Vib. 284 (2005) 757–781, DOI: 10.1016/j.jsv.2004.07.009.

[20] A. Giraudeau, F. Pierron, Identification of material stiffness and damping in vibrating plates using full-field measurements, J. Phys.: Conf. Ser. 181 (2009) 012063, DOI: 10.1088/1742-6596/181/1/012063.

[21] M. Grédiac, E. Toussaint, F. Pierron, Special virtual fields for the direct determination of material parameters with the virtual fields method. 1—Principle and definition, Int. J. Solids Struct. 39 (2002) 2691–2705, DOI: 10.1016/S0020-7683(02)00127-0.

[22] M. Grédiac, E. Toussaint, F. Pierron, Special virtual fields for the direct determination of material parameters with the virtual fields method. 2—Application to in-plane properties, Int. J. Solids Struct. 39 (2002) 2707–2730, DOI: 10.1016/S0020-7683(02)00128-2.

[23] M. Grédiac, E. Toussaint, F. Pierron, Special virtual fields for the direct determination of material parameters with the virtual fields method. 3. Application to the bending rigidities of anisotropic plates, Int. J. Solids Struct. 40 (2003) 2401–2419, DOI: 10.1016/S0020-7683(03)00030-1.

[24] C. Kim, J.-H. Kim, M.-G. Lee, A virtual fields method for identifying anisotropic elastic constants of fiber reinforced composites using a single tension test: Theory and validation, Compos B Eng 200 (2020) 108338, DOI: 10.1016/j.compositesb.2020.108338.

[25] T. Nguyen, J. Huntley, I. Ashcroft, P. Ruiz, F. Pierron, A Fourier-series-based virtual fields method for the identification of 2-D stiffness distributions: A Fourier Virtual Fields Method to identify stiffness distributions, Int. J. Numer. Meth. Engng (12) (2014), Number: 12 917–936, DOI: 10.1002/nme.4665.

[26] J.-H. Kim, F. Pierron, M. Wisnom, K. Syed-Muhamad, Identification of the local stiffness reduction of a damaged composite plate using the virtual fields method, Compos Part Appl Sci Manuf 38 (2007) 2065–2075, DOI: 10.1016/j.compositesa.2007.04.006.

[27] S. Avril, M. Grédiac, F. Pierron, Sensitivity of the virtual fields method to noisy data, Comput Mech 34 (2004) 439–452, DOI: 10.1007/s00466-004-0589-6.

[28] A. Giraudeau, F. Pierron, B. Guo, An alternative to modal analysis for material stiffness and damping identification from vibrating plates, J. Sound Vib. 329 (2010) 1653–1672, DOI: 10.1016/j.jsv.2009.11.031.

[29] N. Connesson, E. Clayton, P. V. Bayly, F. Pierron, Extension of the Optimised Virtual Fields Method to Estimate Viscoelastic Material Parameters from 3D Dynamic Displacement Fields, Strain 51 (2015) 110–134, DOI: 10.1111/str.12126.

[30] A. Marek, F. M. Davis, F. Pierron, Sensitivity-based virtual fields for the non-linear virtual fields method, Comput Mech 60 (2017) 409–431, DOI: 10.1007/s00466-017-1411-6.

[31] A. Berry, O. Robin, F. Pierron, Identification of dynamic loading on a bending plate using the Virtual Fields Method, J. Sound Vib. 333 (2014) 7151–7164, DOI: 10.1016/j.jsv.2014.08.038.

[32] A. Berry, O. Robin, Identification of spatially correlated excitations on a bending plate using the Virtual Fields Method, J. Sound Vib. 375 (2016) 76–91, DOI: 10.1016/j.jsv.2016.03.042.

[33] P. O'Donoughue, O. Robin, A. Berry, Time-space identification of mechanical impacts and distributed random excitations on plates and membranes, Proc. Inst. Mech. Eng. C 233 (2019) 6436–6447, DOI: 10.1177/0954406219839094.

[34] P. O'Donoughue, O. Robin, A. Berry, Time-resolved identification of mechanical loadings on plates using the virtual fields method and deflectometry measurements, Strain 54 (2018) e12258, DOI: 10.1111/str.12258.

[35] N. Madinier, Q. Leclère, K. Ege, A. Berry, Development of a Frequency-Adapted Virtual Fields Method as an alternative to the Corrected Force Analysis Technique for dynamic forces and structural parameter identification, J. Sound Vib. 573 (2024) 118220, DOI: 10.1016/j.jsv.2023.118220.

[36] C. Pézerat, Méthode d'identification des efforts appliqués sur une structure vibrante, par résolution et régularisation du problème inverse (Method of identification of forces applied on a vibrating structure, by resolution and regularization of the inverse problem), PhD thesis, Institut National des Sciences Appliquées de Lyon, 1996, 134 pages.

[37] F. Pierron, M. Grédiac, The Virtual Fields Method: Extracting Constitutive Mechanical Parameters from Full-field Deformation Measurements, Springer-Verlag, New York, 2012, 531 pages, ISBN: 978-1-4614-1823-8, DOI: 10.1007/978-1-4614-1824-5.

[38] Y. Mei, J. Deng, X. Guo, S. Goenezen, S. Avril, Introducing regularization into the virtual fields method (VFM) to identify nonhomogeneous elastic property distributions, Comput Mech 67 (2021) 1581–1599, DOI: https://doi.org/10.1007/s00466-021-02007-3.

[39] D. Varsamis, N. Karampetakis, On the Newton bivariate polynomial interpolation with applications, Multidim Syst Sign Process 25 (1) (2014) 179–209, DOI: 10.1007/s11045-012-0198-z.

[40] D. Varsamis, N. Karampetakis, P. Mastorocostas, An Optimal Bivariate Polynomial Interpolation Basis for the Application of the Evaluation-Interpolation Technique, Appl. Math. Inf. Sci. 8 (1) (2014) 117–125, DOI: 10.12785/amis/080114.

[41] E. G. Williams, Continuation of acoustic near-fields, J. Acoust. Soc. Am. 113 (3) (2003) 1273–1281, DOI: 10.1121/1.1528173.